catalysts

MDPI

Review

# Advances in Nanostructured Metal-Encapsulated Porous Organic-Polymer Composites for Catalyzed Organic Chemical Synthesis

**Wilhemina Sebati [1,2] and Suprakas Sinha Ray [1,2,*]**

[1] DST-CSIR National Centre for Nanostructured Materials, Council for Scientific and Industrial Research, Pretoria 0001, South Africa; wsebati@csir.co.za

[2] Department of Applied Chemistry, University of Johannesburg, Doornfontein, Johannesburg 2028, South Africa

* Correspondence: rsuprakas@csir.co.za or ssinharay@uj.ac.za; Tel.: +27-012-841-2388

Received: 7 September 2018; Accepted: 19 October 2018; Published: 24 October 2018


**Abstract:** Porous organic polymers (POPs) are of growing research interest owing to their high surface areas, stabilities, controllable chemical configurations, and tunable pore volumes. The molecular nanoarchitecture of POP provides metal or metal oxide binding sites, which is promising for the development of advanced heterogeneous catalysts. This article highlights the development of numerous kinds of POPs and key achievements to date, including their functionalization and incorporation of nanoparticles into their framework structures, characterization methods that are predominantly in use for POP-based materials, and their applications as catalysts in several reactions. Scientists today are capable of preparing POP-based materials that show good selectivity, activity, durability, and recoverability, which can help overcome many of the current environmental and industrial problems. These POP-based materials exhibit enhanced catalytic activities for diverse reactions, including coupling, hydrogenation, and acid catalysis.

**Keywords:** porous organic polymers; rigid framework; heterogeneous nanocatalysis; nanoparticles; catalytic performance

## 1. Introduction

Because of their high chemical activities and extensive applications, the assembly of nanoporous materials with metal and metal oxide nanoparticles has opened up research areas aimed at the development of new heterogeneous catalysts [1–4]. The properties of the nanoparticles, such as type of support, morphology, and size distribution, affect the catalytic activity of such nanoporous materials [5]. Unlike large nanoparticles and bulk-metal particles, ultrafine metal nanoparticles exhibit unique properties. They are allegedly more reactive in catalysis because smaller particles result in high surface-to-volume ratios and in turn provide a large number of available active sites for substrates to react [6–9]. Owing to the high surface energies, ultrafine metal nanoparticles are likely to aggregate and leach during the course of a catalytic reaction, leading to loss of catalytic activity and poor recyclability [10]. To address these problems, a variety of molecular architectures—including porous organic polymers (POPs) [11–19], metal-organic frameworks (MOFs) [20,21], and covalent organic frameworks (COFs)-have been proposed as useful platforms for the fabrication and encapsulation of nanoparticles [22,23], as well as for catalyst positioning, due to their porous nature and relatively large surface areas. However, it should be noted that MOFs and COFs are unstable in acidic, basic, or moist environments due to the coordination bonds in MOFs and the boronate ester or imine groups present in COFs, which hinder their use in catalysis [24]. In comparison, POPs are more

chemically robust and hydrothermally stable. This study focuses on POPs, as they are easiest to make and are more stable than MOFs and COFs. POPs are stable, noncrystalline, and have high surface area which plays an important role in catalysis.

This review emphasizes methods and techniques used to characterize, synthesize, and analyze functionalized and metal-encapsulated POP nanocatalysts, and their applications in a variety of catalytic reactions.

## 2. Overview of Nanostructured Metal-Encapsulated Porous Organic-Polymer Catalysts

POPs have emerged as a favorable molecular nanoarchitecture for the immobilization of ultrafine metal nanoparticles. Their fabrication, encapsulation, and stabilization are facilitated by their large surface areas with distinctly dispersed pore sizes, thermally and chemically stable bonds, low structural densities, and the presence of hydrophobic components in their structures. These POP characteristics contribute to their high catalytic activity and stability. The pore is the central structural motif in porous materials as it provides accessible space for quests where chemical reactions or physical sorption can take place. Porous materials can be selectively synthesized, assembled, or constructed for molecules and they should form continuous communicating pore passages [25,26]. Microporous polymeric materials of different types have been denoted by many different names, such as benzene-benzylamine (BBA), divinylbenzene-acrylic acid (DVAC), triazine-based polymers (TRIA), divinyltriallyamine (DVTA), organic ionic polymers (OIP), click-based porous organic polymers (CPPs), pyrene-based porous organic polymers (PPOP), polytriphenyl amine porous polymer (PPTPA), polymers of intrinsic microporosity (PIMs), conjugated microporous polymers (CMPs), and porous aromatic frameworks (PAFs). These materials are amorphous but typically possess relatively high internal surface areas attributed to micro mesopores that are constructed from rigid and multitopic building blocks [11]. Porous materials have potential applications in gas storage, pharmaceuticals, environment, and catalysis and only materials that focus on catalyzed organic synthesis will be discussed. Catalytic active sites in POP materials can be controlled, tuned, and modified with different monomers. Metal nanoparticles encapsulated in these POPs are stable and have enhanced catalytic activity due to interactions between the organic linkers in the POP and the metal nanoparticles, which can be improved by the addition of groups that coordinate to metal precursors. Moreover, the easy recovery and recyclability of these heterogeneous catalysts have attracted research interest for the production of fine chemicals and value-added products in the petroleum-refining and chemical industries [27–29].

## 3. Design Strategies for Metal-Encapsulated Porous Organic-Polymer Nanocatalysts

The surface areas and pore sizes of porous materials can be modified by incorporating building blocks (monomers) with specific shapes and sizes for specific applications. In general, porous organic materials can be functionalized in either a pre-synthetic (bottom-up) or post-synthetic (top-down) manner [30,31]. The pre-synthesis method involves the functionalization of building blocks followed by polymerization such that monomers are transformed into porous organic materials [30], whereas the post-synthesis method involves modification of the initially synthesized porous organic materials, which is effective for the incorporation of numerous functional groups in the porous organic material and useful for advanced applications [31]. Pre-synthetic functionalization can introduce functional groups that hinder polymerization; thus, post-synthetic functionalization is required under these circumstances.

In the late 1990s, the synthesis of high-valence microporous organic-polymer materials with complex structures was attempted in order to create pores with better molecular features [32]. Pores were also formed through the use of slower bond-developing reactions such that they matched the sizes of the guest particles [33]. Macroporous polymers are traditionally synthesized by interconnecting polymerized long-chain monomers with ditopic cross linkers [34], whereas POPs are generally synthesized

using multitopic monomer units, and permanent microporosity can only be achieved when they are constructed from moderately rigid monomers that produce pores with rigid walls when cross-linked [35].

A number of recent bond-forming processes, rather than traditional methods, have been used to synthesize POPs with varied structural frameworks [34,35]. Metal-catalyzed coupling reactions—including Yamamoto [36–38], Sonogashira-Hagihara [39], oxidative couplings [40], Suzuki-Miyaura [41], Friedel-Crafts alkylations [42–44], nitrile cyclotrimerization [45,46], terminal alkyl trimerizations [47,48], olefin metathesis [49], and click reactions [50]—are well known and provide opportunities for the synthesis of POPs with structures that suit a variety of roles. Irrespective of the rapid progress toward the synthesis of POPs, the development of polymerization protocols that are environmentally beneficial and economical remains a long-term goal. To date, the development of porous organic-polymer-supported materials with encapsulated metal or metal oxide nanoparticles in their interior or exterior cavities has been the focus of attention. Metal-encapsulated porous organic-polymer nanocatalysts are usually synthesized by the post-modification of POP supports with metal-nanoparticle precursors in the presence of an oxidizing agent. Tables 1 and 2 summarize literature reports that describe the syntheses of various POP supports and their post-modifications with metal nanoparticles and various functional groups, whereby the synthetic procedures are further shown in reaction , Scheme 1, Scheme 2, Scheme 3, Scheme 4, Scheme 5, Scheme 6, Scheme 7, Scheme 8, Scheme 9, Scheme 10. Some of the reactions take place either at high temperatures, use hazardous chemicals, or require long times for product formation. Therefore, sustainable, simple, and low-cost methodologies for the preparation of POP-based materials need to be developed.

**Table 1.** Synthesis of porous organic polymers.

| POP Material | Preparation Method | Reactants | Temp. (°C) | Time (h) | Solvent | Ref. |
|---|---|---|---|---|---|---|
| BBA | Friedel-crafts alkylation | Benzene<br>Benzylamine<br>Formaldehyde dimethyl acetal | 80 | 20 | Methanol | [51] |
| DVAC | Non-aqueous polymerization | 1,4-divinyl benzene<br>Acrylic acid<br>Azobisisobutyronitrile | 120 | 24 | Acetone | [52] |
| TRIA | Non-aqueous polymerization | 1,4-divinyl benzene<br>Azobisisobutyronitrile<br>2,4,6-triallyoxy-1,3,5-triazine | 120 | 24 | Acetone | [53,54] |
| DVTA | Polymerization | 1,4-divinyl benzene<br>Triallylamine<br>Azobisisobutyronitrile | 120 | 24 | Acetone | [55] |
| OIP | Suzuki–Miyaura cross coupling | 1,3-bis(4-bromophenyl) imidazoli-um bromide<br>1,3,5-tri(4-pinacholatoborolanephenyl) benzene | 110 | 48 | 1,4-dioxane | [56] |
| CPP-C | Click reaction | 4,4′-diazidobiphenyl<br>$CuSO_4 \cdot 5H_2O$<br>1,3,5-triethynylbenzene<br>Sodium ascorbate | 100, under $N_2$ | 72 | DMF | [57] |
| CPP-Y | Yamamoto | Bis(1,5-cycloctadine)-nickel(0)<br>2,2′-bipyridyl<br>1,5-cycloctadiene<br>1,3,5-tris(1-(4-bromophenyl)-1H-1,2,3-triazol-4-yl)-benzene | 80 | 72 | DMF | [57] |
| CPP-1 | Click reaction | Tetrakis-(4-ethylpnyhenyl)methane<br>4,4′-diazidobiphenyl<br>$CuSO_4 \cdot 5H_2O$<br>Sodium ascorbate | 100 | 72 | DMF | [58] |
| CPP-2 | Click reaction | Tetrakis-(4-azidophenyl)methane<br>4,4′-diethynylphenyl<br>$CuSO_4 \cdot 5H_2O$<br>Sodium ascorbate | 100 | 72 | DMF | [58] |

**Table 1.** *Cont.*

| POP Material | Preparation Method | Reactants | Temp. (°C) | Time (h) | Solvent | Ref. |
|---|---|---|---|---|---|---|
| CPP-F1 | Click reaction | 1,4-bis(azidomethyl)benzene<br>1,3,5-triethynyl-benzene<br>Sodium ascorbate<br>$CuSO_4 \cdot 5H_2O$<br>Diisopropylethylamine | 60, under $N_2$ | 72 | THF | [59] |
| CPP-F2 | Click reaction | 1,4-bis(azidomethyl)benzene<br>Tetrakis-(4-ethynylphenyl)methane<br>Sodium ascorbate<br>$CuSO_4 \cdot 5H_2O$<br>Diisopropylethylamine | 60 | 72 | THF | [59] |
| PPOP 1, PPOP 2, PPOP 3 | Friedel-crafts alkylation | Bis(1,4-bromomethyl)benzene<br>Pyrene<br>Anhydrous ferric chloride | 80 | 20 | 1,2-Dichloroethane | [60] |
| PPTPA | One-step Oxidative polymerization | Triphenylamine<br>Anhydrous ferric chloride | 25, under $N_2$ | 20 | Dichloroethane | [61,62] |
| POP 1, POP 2 | Click reaction | 1,3,5-tris(4-azidophenyl)-benzene<br>2,6-diethynylpyridine<br>Methyl-2,6-diethynylisonicotinate<br>Sodium ascorbate<br>$CuSO_4 \cdot 5H_2O$ | 100, under $N_2$ | 72 | DMF | [63] |

**Table 2.** Synthesis of functionalized and metal nanoparticles-encapsulated POPs.

| Material | Reactants | Reducing Agent | Temperature (°C) | Time (h) | Solvent | Ref. |
|---|---|---|---|---|---|---|
| Ru-BBA | BBA POP<br>$RuCl_3 \cdot 3H_2O$ | $NaBH_4$<br>Ethylene glycol | 25<br>180 | 28<br>3 | MeOH | [51] |
| Cu-B | DVAC POP<br>$CuCl_2 \cdot 2H_2O$ | Hydrazine hydrate | 80 | 6 | NaOH | [52] |
| Pd@Tria | Tria POP<br>$Pd(OAc)_2$<br>Sodium acetate | $NaBH_4$ | 25 | 26 | MeOH | [53] |
| Mn@DVTA | DVTA POP<br>$KMnO_4$ | Ethylene glycol | 80, 120, 160 | 6 | Water | [55] |
| $Mn_3O_4$@POP | Triazine-based POP<br>$Mn(OAc)_2 \cdot 4H_2O$ | $NH_4OH$ | 160 | 3 | $NH_3$ solution | [54] |
| Pd@OIP | OIP POP<br>$Pd(PPh_3)_4$ | $K_3CO_2$ | 110 | 48 | DMF<br>1,4-dioxane | [56] |
| Pd@CPP-C, Pd@CPPY | CPP-C, CPP-Y<br>$Pd(OAc)_2$ | $H_2/N_2$ | 200 | 4 | DCM | [57] |
| Pd@CPP1, Pd@CPP2 | CPP1, CPP2<br>$Pd(OAc)_2$ | $H_2/N_2$<br>$NaBH_4$ | 200<br>80 | 4<br>12 | DCM | [58] |
| Pd@CPPF1<br>Pd@CPPF2 | CPPF1,<br>CPPF2$Pd(OAc)_2$ | - | 60 | 24 | Acetone | [59] |
| SPPOP 1, SPPOP 2, SPPOP 3 | PPOP1, PPOP2, PPOP3<br>Chlorosulfonic acid | - | 25 | 48 | DCM | [60] |
| SPPTPA-1 | PPTPA<br>Chlorosulfonic acid | - | 25 | 72 | DCM | [61] |
| Pd/$Fe_3O_4$-PPTPA-1 | PPTPA<br>$PdCl_2$<br>$FeCl_3$<br>Trisodium citrate | Ethylene glycol | 200 | 8 | Ethylene glycol | [62] |
| Pd@POP1, Pd@POP2, Pd@POP3 | POP1, POP2, POP3<br>$Pd(OAc)_2$ | $NaBH_4$ | 25 | 3 | DCM | [63] |

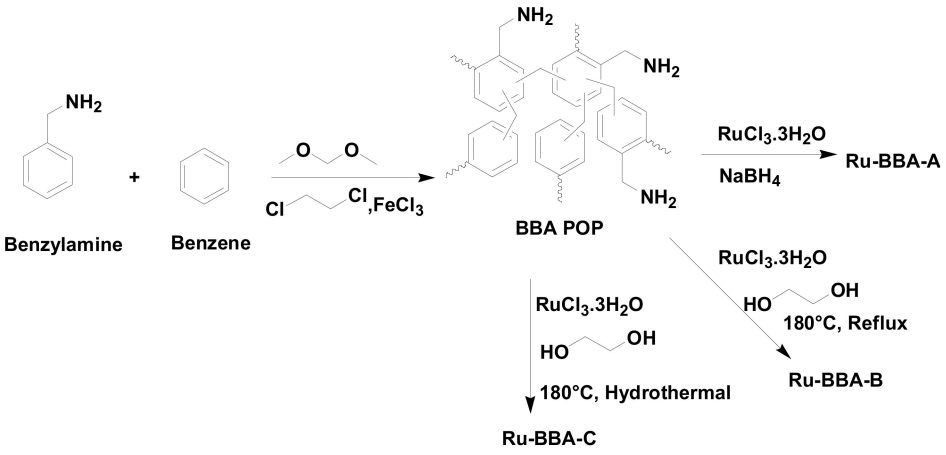


**Scheme 1.** Synthesis of nanoporous organic polymer BBA and Ru@BBA nanocatalysts.

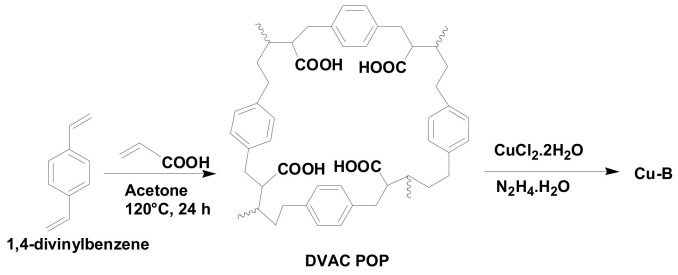


**Scheme 2.** Synthesis of DVAC porous organic polymer and Cu@DVAC nanocatalyst.

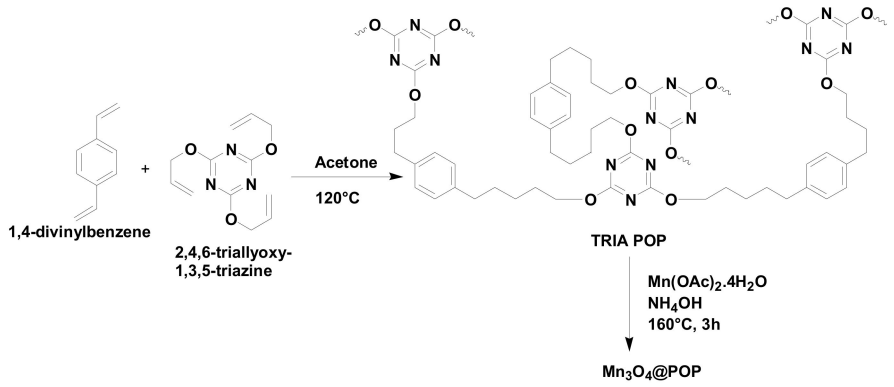


**Scheme 3.** Synthesis of TRIA-based organic polymer and $Mn_3O_4$@POP nanocatalyst.

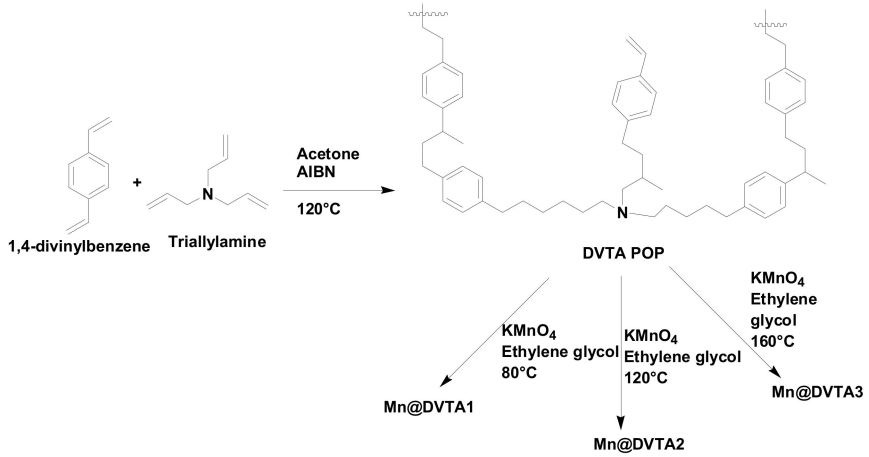


**Scheme 4.** Synthesis of DVTA polymer and Mn@DVTA nanocatalysts.

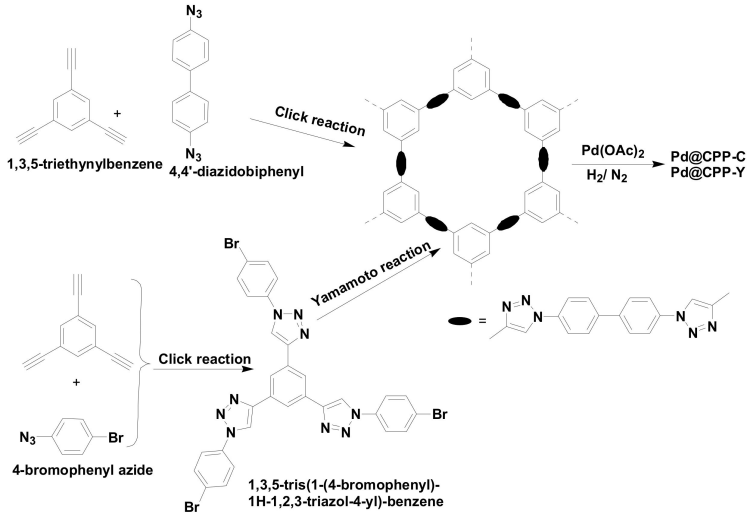


**Scheme 5.** Synthesis of CPPC, CPP-Y polymers, Pd@CPP-C, and Pd@CPP-Y nanocatalysts.

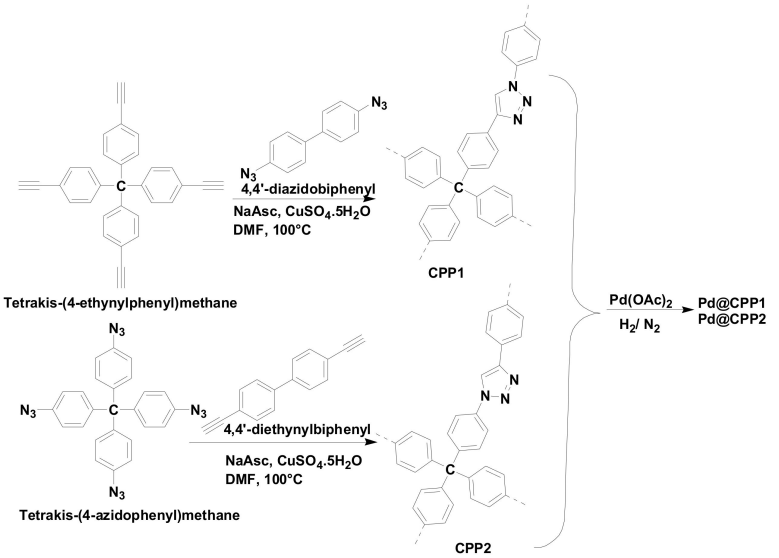


**Scheme 6.** Synthesis of CPP1, CPP2 polymers, and Pd@CPP nanocatalysts.

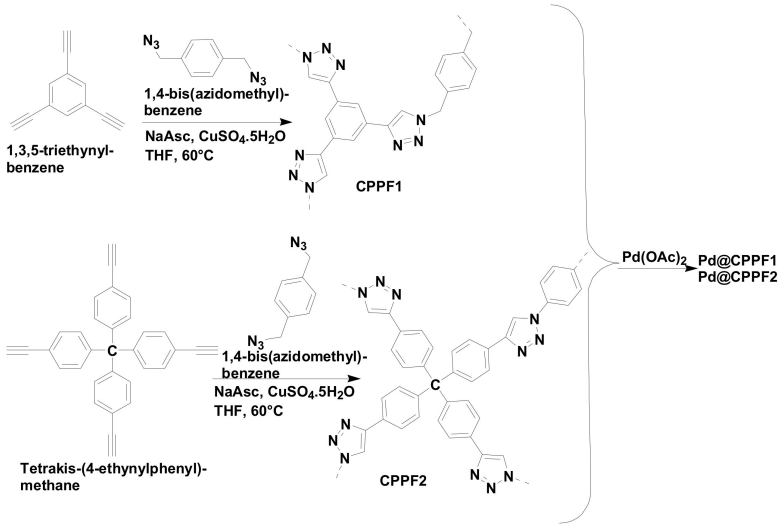


**Scheme 7.** Synthesis of CPPF1 and CPPF2 and their corresponding palladium-containing polymers.

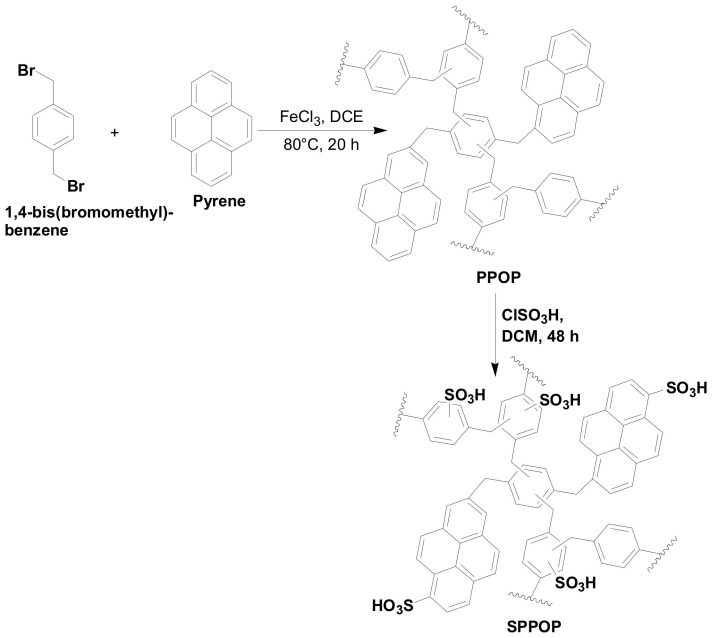


**Scheme 8.** Synthesis of PPOP polymer and its functionalization with chlorosulfonic acid.

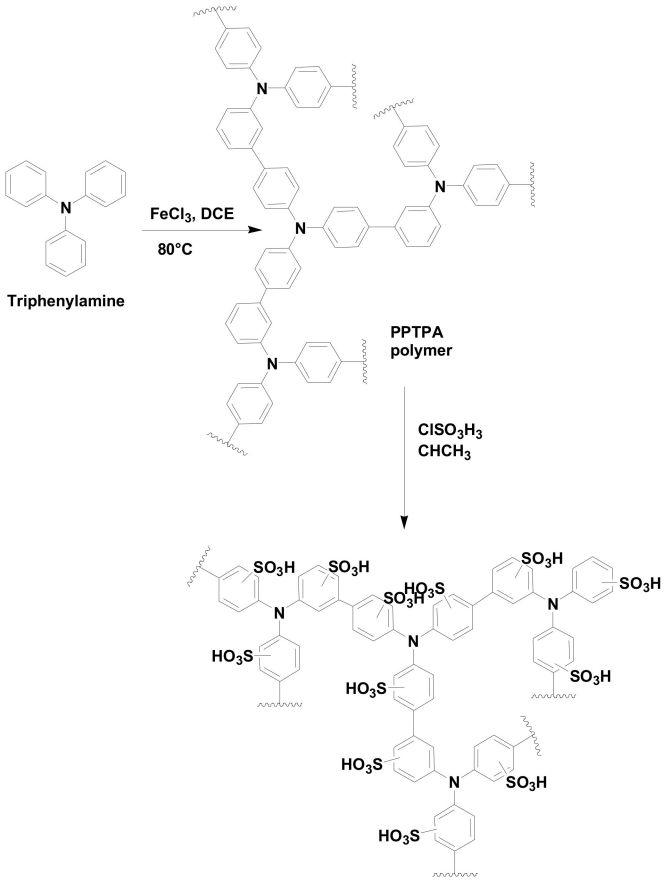


**Scheme 9.** Synthesis of PPTPA polymer and its functionalization with chlorosulfonic acid.

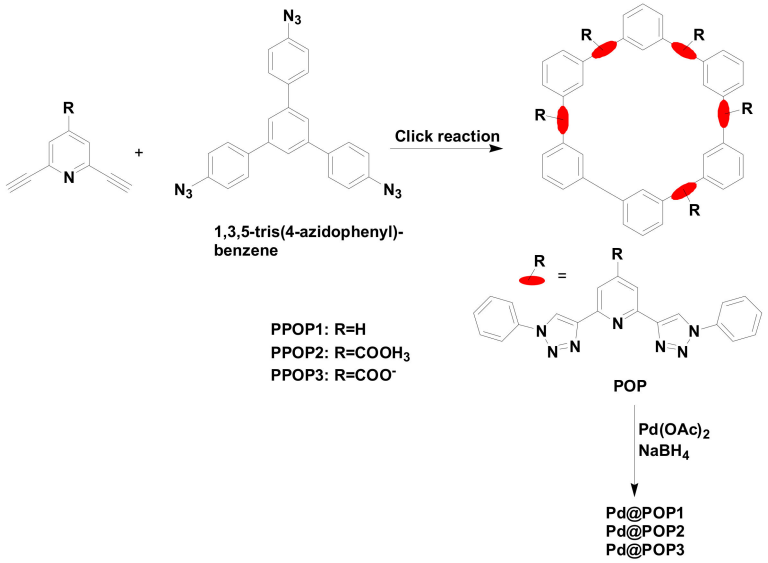


**Scheme 10.** Synthesis of POP1, POP3, POP3 polymers, and their corresponding palladium incorporated catalysts.

## 4. Characterization of Metal-Encapsulated and Functionalized Porous Organic-Polymer Nanocatalysts

The availability of characterization techniques for catalysts is representative of the incredible difference between catalysis technology present in the 1950s and 1960s and that present today. A number of factors, such as better catalyst control that facilitates the optimization of existing processes and recognition of new processes and catalysts as well as their unusual characteristics of catalysts, have contributed to the growth in catalysis technology. A variety of characterization methods have been used to investigate the morphologies of pure and metal-encapsulated POPs and to structurally characterize them. These methods include X-ray diffraction (XRD), the Brunnauer-Emmett-Teller (BET) adsorption method, scanning electron microscopy (SEM), transmission electron microscopy (TEM), energy-dispersive X-ray spectroscopy (EDX), X-ray photoelectron spectroscopy (XPS), Fourier-transform infrared (FT-IR) spectroscopy, and thermal gravimetric analysis (TGA).

XRD is a non-destructive and adaptable method that provides information on the crystallographic structure and chemical composition of a material. During XRD, X-ray beams are reflected from parallel atomic layers within the crystal structure of a material over a range of diffraction angles to provide either constructive or destructive interference. Several studies have shown that XRD is an appropriate technique for exploring structures of POP-based materials [64]. The literature reveals that POP supports exhibit broad XRD patterns that show the presence of amorphous phases, while metal-encapsulated POPs exhibit sharp peaks consistent with the presence of crystallized metal nanoparticles inside their polymer frameworks, as shown in Figure 1a,b [52–55]. The amorphous nature of POPs was considered to be a drawback from the perspective of structural analysis; however, XRD is able to swiftly determining the presence of viable materials in a reaction mixture without the need to wait for crystals to form. Moreover, a variety of handles in the POP building blocks can be modified following polymer synthesis to give new POPs with the same structural design but with different functionalities in their pores.

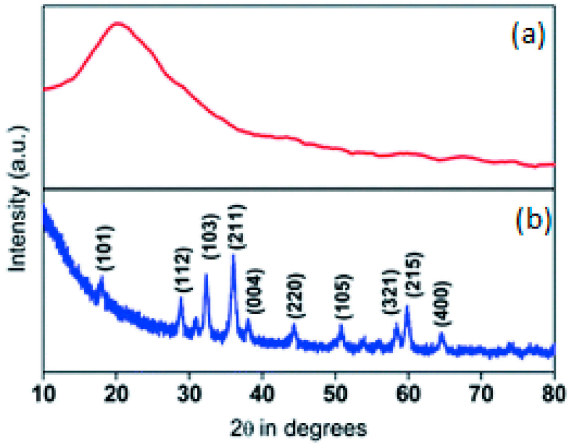


**Figure 1.** XRD patterns of (**a**) a pure POP and (**b**) a metal-encapsulated POP. Reproduced with permission from [54]. Copyright 2016, the Royal Society of Chemistry.

The BET method is the most used technique for determining surface areas and porosities of POP supports and nanocatalysts. The literature reveals that pure and metal-encapsulated POPs exhibit a sharp uptake of $N_2$ in the high $P/P_0$ pressure region (Figure 2) [51–59]. These POPs contain one or more groups of pores, which are classified as micropores (<2 nm), mesopores (<50 nm), or macropores (>50 nm). Table 3 displays the BET surface areas and pore volumes reported for neat porous organic polymers, as well as metal-nanoparticle-incorporated and functionalized POPs. To date, the highest POP BET surface area used in heterogeneous catalysis was reported by Mondal et al. [61] to be 1437 $m^2 \cdot g^{-1}$, but the material had a low pore volume of 0.881 $cm^3 \cdot g^{-1}$, while the highest pore volume to date was reported by Sudipta et al. [60] to be 1.7 $cm^3 \cdot g^{-1}$, but the associated surface area was low (615 $m^2 \cdot g^{-1}$). Nanofiber folding is responsible for the high surface area and high flexibility of the polymer is responsible for low surface area. The appreciable decreases in the BET surface areas and pore volumes of metal-encapsulated and functionalized POPs compared to those of pure POPs suggest that metal nanoparticles and functional groups were successfully incorporated into the polymer frameworks.

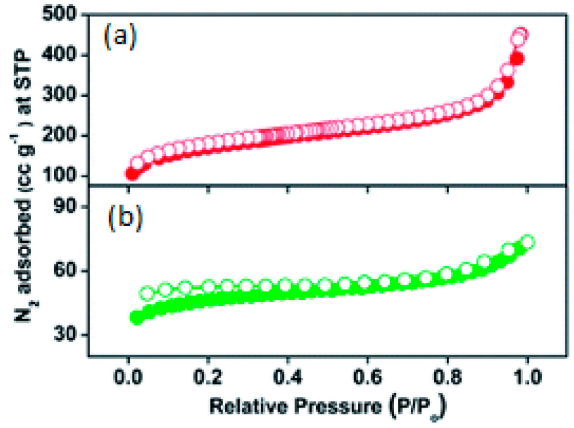


**Figure 2.** Nitrogen adsorption/desorption isotherms for (**a**) a pure POP and (**b**) a metal-encapsulated POP. Reproduced with permission from [54]. Copyright 2016, the Royal Society of Chemistry.

**Table 3.** BET surface areas and porosities of neat, metal encapsulated, and functionalized POPs.

| Material | Surface Area ($m^2/g$) | Pore Volume ($cm^3/g$) | Ref. |
|---|---|---|---|
| BBA-1 | 607.8 | 0.416 | [51] |
| Ru-A | 551.6 | 0.420 | |
| Ru-B | 523.2 | 0.387 | |
| Ru-C | 543.3 | 0.431 | |
| DVAC | 420 | 1.270 | [52] |
| Cu-B | 260 | 0.703 | |
| TRIA | 620 | 0.510 | [53] |
| Pd@TRIA1 | 573 | 0.460 | |
| Pd@TRIA2 | 459 | 0.320 | |
| Mn@DVTA1 | 546 | 0.548 | [55] |
| Mn@DVTA2 | 656 | 0.459 | |
| Mn@DVTA3 | 948 | 0.548 | |
| TRIA | 620 | 0.510 | [54] |
| $Mn_3O_4$@POP | 178 | 0.169 | |
| CPP-C | 156 | 0.190 | [57] |
| Pd@CPPC | 43 | 0.110 | |
| CPP-Y | 408 | 0.250 | |
| Pd@CPPY | 70 | 0.070 | |
| CPP1 | 826 | 0.300 | [58] |
| Pd@CPP1 | 444 | 0.200 | |
| CPP2 | 894 | 0.63 | |
| Pd@CPP2 | 323 | 0.52 | |
| CPP-F1 | 12 | - | [59] |
| CPP-F2 | 28 | - | |
| PPOP-1 | 615.0 | 1.700 | [60] |
| SPPOP-1 | 280.0 | 1.680 | |
| PPTPA-1 | 1437.0 | 0.881 | [61] |
| SPPTPA-1 | 737.0 | 0.338 | |
| POP1 | 358.0 | 0.160 | [63] |
| POP2 | 106.0 | 0.035 | |
| POP3 | 79.0 | 0.030 | |
| Pd@POP1 | 263.0 | - | |
| Pd@POP2 | 72.0 | - | |
| Pd@POP3 | 50.0 | - | |

SEM is proficient at creating high-resolution images of the surface of samples. These images have distinctive 3-D appearances due to the manner in which they are created [65,66]. On the other hand, TEM is a nanoscale imaging tool that transmits a beam of electrons through the sample to form an image that is enlarged and directed for display on a fluorescent screen or on a photographic film layer for detection by a sensor [67,68]. Generally, TEM resolution is higher than that of SEM; however, SEM is capable of imaging bulk samples with greater depths of view because it is dependent on surface processes rather than transmission [64]. SEM and TEM have been used to acquire data about the shapes, sizes, homogeneities, and contemporary presence of the amorphous and crystalline phases of MNP-encapsulated POPs. Figures 3 and 4 respectively show SEM and TEM images of a metal-nanoparticle-encapsulated POP. These images provide information about the shapes, sizes, and homogeneities of the nanoparticles on the surface and interior cavities of the POP support. The MNP-encapsulated POPs display homogenous dispersions of MNPs on the surfaces and in the interior cavities of the nanoporous polymers. Mondal et al. [51,52] reported TEM images of ruthenium (Ru-A) and copper (Cu-B) encapsulated POPs, which revealed Ru and Cu nanoparticles 3.5–7.0 nm and 9.8–14.3 nm in size, respectively, which exhibit a certain amount of agglomeration. This suggests

that nitrogen-rich polymers are unable to completely inhibit aggregation on the outer surfaces of the nanoparticles through Oswald ripening; Cu nanoparticles interact strongly with the–COOH groups on the surface of the nanoporous DVAC-1 polymer. FE-SEM images revealed that the morphology of Cu-B resembled sea-urchin-like copper-polymer nanostructures of thin needles [52]. Ru-B and Ru-C also exhibited Ru nanoparticles that are 1.5–4.0 nm and 2.0–4.0 nm in size, respectively, which are too small to be easily incorporated into the interior cavities of the nanoporous BBA-1 polymer. During the synthesis of Ru-B and Ru-C, ethylene glycol was used as the reducing agent, which acted as a stabilizer that controlled particle growth and inhibited aggregation [51]. Borah et al. [55] reported $Mn_3O_4$ nanoparticles that were homogeneously dispersed over the surface of the DVTA polymer on the basis of TEM images of Mn@DVTA1, while a nanowire-like morphology of $Mn_3O_4$ nanomaterials, with an average length of 0.8 mm, was observed for Mn@DVTA2 and Mn@DVTA3; these nanowires were revealed to fuse, even at high temperatures, to form octahedral $Mn_3O_4$ particles. Singuru et al. [62] used TEM to observe monodispersed needle-like $Mn_3O_4$ NPs with widths in the 30–250 and 7–12 nm ranges that were firmly surrounded by a porous organic polymer with a 3D flame-like form composed of an interconnected 3D porous network, while flake-like irregular blocks with rough surfaces of aggregated nanoparticles were observed in the SEM images of the as-synthesized POP and $Mn_3O_4$@POP [54]. Ultrafine palladium nanoparticles, with average sizes of 1.69 ± 0.33, 1.39 ± 0.31, 1.45 ± 0.36, and 1.43 ± 0.34 nm, were homogeneously distributed in Pd@CPPC, Pd@CPPY, Pd@CPP1, and Pd@CPP2; these particles were small enough to be housed in the internal cavities of the polymer networks [57,58]. SEM images also revealed that the original CPP1, CPP2, CPP-F1, and CPP-F2 morphologies remained intact following encapsulation of the palladium nanoparticles [58,59]. CPP-F1 has a 3D network that differs from the usual granular morphology reported for most robust POPs prepared from triangular monomers, whereas, CPP-F2 consisted of quite uniform granules with particles 100–200 nm in size, in agreement with the morphologies reported for polymers construction using tetrahedral building blocks [59]. Kundu and Bhaumik [60] reported TEM images of PPOP1, which exhibited a nanofiber-like morphology with widths of 80–120 nm and length of 5 μm, whereas the sulfonated SPPOP1 polymer retained the nanofibrous morphology of PPOP1 after sulfonation; however, the sulfonated SPPOP3 polymer displayed a spherical morphology with diameters of 0.5–1.2 μm. SEM images suggested increased nanofiber widths following sulfonation, and the images of PPOP2, SPOP2, PPOP3, and SPPOP3 revealed that the nanofiber-like polymer particles reformed spherical nanoparticles following sulfonation [60]. The SEM and TEM images of PTPPA and SPPTPA reported by Mondal et al. [61] also suggested an increase in nanofiber diameter following sulfonation of the aromatic rings of PPTPA1. Triphenylamine molecules also act as capping agents for Fe (III) ions adsorbed onto monomer surfaces, which inhibited the lateral growth of the polymer and led to 1D self-assembly. No template, surfactant, or structure-directing agent was required to advance this nanofiber-like morphology, and secondary overgrowth, which leads to the formation of agglomerated particles, was inhibited during the reaction.

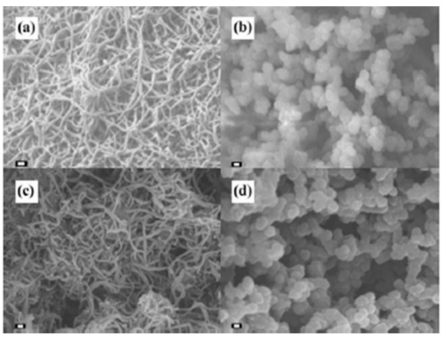


**Figure 3.** SEM images of (**a**,**b**) neat POPs and (**c**,**d**) metal-nanoparticle-encapsulated POPs. Reproduced with permission from [59]. Copyright 2014, Springer Nature.

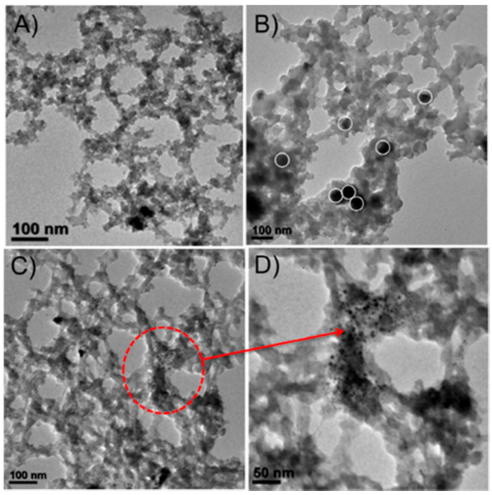


**Figure 4.** (**A**–**D**) TEM images of metal-nanoparticle-encapsulated POPs. (**D**) is the magnified portion of (**C**). Reproduced with permission from [52]. Copyright 2015, Springer Nature.

EDX and XPS techniques provide information on the elemental composition and chemical status of a solid surface before and after a chemical reaction. They provide data through the ejection of electrons from the solid material and the analysis of their related energies. EDX and the elemental maps of MNP-encapsulated POPs reveal the successful incorporation and homogeneous distributions of MNPs on POP supports [51–59]. The amount of sulfonation of a sulfonated POP can also be obtained through elemental analysis by determining the weight-percentage of sulfur [60]. The XPS spectra of Ru-incorporated POPs reveal C 1s and N 1s binding-energy peaks, as well as a new peak that corresponds to the Ru 3p binding energy of ruthenium nanoparticles in their zero oxidation state, as shown in Figure 5. The Ru 3p binding energy of Ru-A appeared at a higher energy than those of Ru-B and Ru-C, which is attributed to solid interactions between the polymer network and the Ru nanoparticles, suggesting that electron transfer from the metal to the organic linkers results in a moderately positively charged metal phase ($Ru^{\delta+}$). In contrast to Ru-A, the Ru 3p binding energies of Ru-B and Ru-C differed only by about 1.2 eV, which could be possibly attributed to interactions with the–OH groups of ethylene glycol on the surface that alters the electron densities of Ru nanoparticles in these materials [51]. The Cu–B spectrum exhibited a $2p_{3/2}$ binding energy along with another strong $2p_{1/2}$ binding-energy peak, indicating that the Cu in the nanoparticles inside the porous channels exists as $Cu^0$, with no signals corresponding to $Cu^{2+}$ observed in the spectra [52].

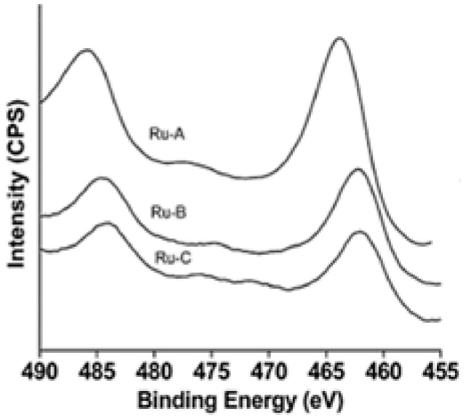


**Figure 5.** Ru 3p XPS spectra of ruthenium-encapsulated POPs. Reproduced with permission from [51]. Copyright 2015, WILEY-VCH Verlag GmbH & Co., Weinheim, Germany.

The spectra of Mn@DVTA displayed peaks corresponding to Mn 2p, while Mn@DVTA-1 exhibited a binding energy of 640 eV, which lies between typical Mn $2p_{1/2}$ and Mn $2p_{3/2}$ values and corresponds to MnO NPs, while the binding energy of the manganese 2p orbitals of Mn@DVTA2 and Mn@DVTA3 were observed at 641 and 642 eV, respectively, which indicates the existence of $Mn_3O_4$, consistent with the presence of copper nanoparticles in the form of $Cu^0$ inside the porous channels and the lack of $Cu^{2+}$ spectral signals [52,55].

The Mn $2p_{1/2}$ binding-energy peak of Mn@DVTA3 was shifted to a higher value than usual, which is attributable to strong interactions between the polymer network and Mn-O that resulted in a more electron deficient $Mn^{3+}$ species [55]. The presence of $Mn_3O_4$ NPs was also confirmed by XPS spectroscopy; $Mn_3O_4$@POP exhibited peaks corresponding to Mn 2p, N 1s, and Mn 3s in its spectrum, in which the Mn 2p peak was split by 11.5 eV into Mn $2p_{1/2}$ and Mn $2p_{3/2}$ peaks that correspond to the NPs. The XPS binding energy of the Mn 2p region of the $Mn_3O_4$@POP hybrid was shifted to lower energies than usual, which is ascribable to strong electronic interactions between the nitrogen-rich porous polymer skeleton and the manganese centers, while the N 1s binding energy was shifted to more-positive values, signifying strong coordination of the manganese centers to the pyridinic nitrogen atoms of the polymer skeleton [54].

The XPS spectra of palladium-incorporated POPs, such as Pd@CPPC, Pd@CPPY, Pd@CPP1, Pd@CPP2, Pd@CPPF1, and Pd@CPPF2 exhibited typical Pd 3d binding-energy peaks, which confirm the successful incorporation of palladium nanoparticles in these POPs. The Pd 3d spectra presented two sets of doublets that correspond to Pd $3d_{5/2}$ and Pd $3d_{3/2}$, with the Pd $3d_{5/2}$ peak attributed to both $Pd^0$ and $Pd^{2+}$ species in the palladium-incorporated POPs. The $Pd^0/Pd^{2+}$ ratios in Pd@CPPC, Pd@CPPY, Pd@CPP1, Pd@CPP2, Pd@CPPF1, and Pd@CPPF2 were determined to be 0.86, 0.36, 0.56, 0.31, 0.298, and 0.360, respectively. Compared to the N 1s XPS spectra of the neat POPs, slight shifts to higher energy of the characteristic N 1s peaks were observed in the XPS spectra of the palladium-incorporated POPs, owing to the coordination of nitrogen atoms to palladium [57–59]. The XPS spectrum of the sulfonated-POP material (SPPTPA) exhibited four peaks that were assigned to S 2p, C 1s, N 1s, and O 1s. The S 2p region showed a binding-energy peak centered at 168.7 eV that is attributed to the–$SO_3H$ group, which confirms the presence of this group in the polymer [61].

Infrared spectroscopy is a tool that can operate on a broader scale, operating in both transmittance and reflectance modes. The former is preferred as it only requires inexpensive laboratory-made cells and produces spectra devoid of artefacts resulting from reflected light. The use of more complex compounds, in which spectroscopic response becomes increasingly more complex, is not a limitation. In this way it becomes possible to study the interactions of molecules present in the reaction and to obtain more direct information on surface reactivity and reaction mechanism. FT-IR spectroscopy has been used to confirm the formation and incorporation of metal nanoparticles in polymer matrices, as shown in Figure 6. The FT-IR spectra of Mn@DVTA3, Mn@DVTA2, and $Mn_3O_4$@POP feature adsorption bands at 625.7, 497.7, and 444.2 $cm^{-1}$ and 625 and 517 $cm^{-1}$ that confirm the presence of the Mn–O bonds inside the nanoporous polymers [54,55]. The FT-IR spectra of CPPC, CPPY, CPP1, CPP2, CPPF1, and CPPF2 confirmed the formation of the 1,2,3-triazolyl linkage at 1618 and 3133 $cm^{-1}$, as evidenced by the loss of the characteristic terminal-alkyne peaks at 3281 $cm^{-1}$. The spectra of the Pd-encapsulated POPs were very similar to those of the neat POPs, demonstrating that their structures remain intact following palladium-nanoparticle loading; however, the palladium-encapsulated POPs exhibit obvious spectral red-shifts from 1618 to 1576 $cm^{-1}$ that reveal interactions between the 1,2,3-triazolyl units and the palladium nanoparticles [57−59]. The FT-IR spectra of the sulfonated POPs confirm the presence of–$SO_3H$ groups at 1005, 1031, and 1058 $cm^{-1}$, as evidenced by the presence of additional bands compared to the spectra of the neat POPs [60,61].

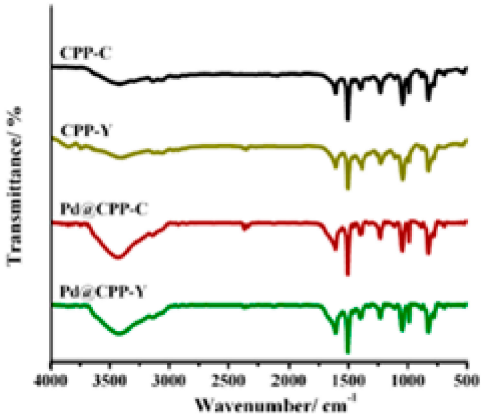


**Figure 6.** FT-IR spectra of neat POPs (CPPC and CPPY) and metal-encapsulated POPs (Pd@CPPC and Pd@CPPY). Reproduced with permission from [57]. Copyright 57, the American Chemical Society.

TGA investigates several kinetic phenomena that occur as the temperature of a solid is changed, as characterized by reabsorption, diffusion into the sample, and heat-transport to the detector, among others. TGA discloses information regarding the losses of volatile components and reactions, such as decomposition, that lead to changes in mass. TGA has revealed that neat, metal nanoparticle encapsulated, and sulfonated POPs are highly thermally stable at temperatures up to 550 °C, as shown in Figure 7 [60,61]. PPOP-1 and SPPOP-1 lost 7% and 25% of their weights when heated to 300 °C and 250 °C, respectively, which is attributed to adsorbed water molecules, while a 52% weight loss was observed for PPOP-1 in the 300–545 °C temperature range due to C–C bond cleavage, and a 68% loss was observed for SPPOP-1 at 250–537 °C due to the decomposition of the framework structure of the material [60]. The PPTPA1 polymer was thermally stable to 515 °C, at which point the porous PPTPA1 framework began to cleave, while SPPTPA-1 first lost weight due to physically adsorbed water molecules followed by strongly adsorbed water molecules that were non-covalently bound to free sulfonic-acid groups. Additional weight losses associated with the free sulfonic acid groups were observed in the 160–270 °C temperature range, while cleavage of the organic structure followed at temperatures above 515 °C [61]. The high thermal stabilities of these nanoporous polymers is attributed to the large number of hyperbranched cross-links and rigid polymer networks in the molecular framework. Mondal et al. [60] performed $NH_3$-TPD analyses of sulfonated POPs in order to understand the nature and strengths of their acidic sites. The levels of sulfonation in the SPPOP1, SPPOP2, and SPPOP3 sulfonated materials were 30, 39, and 44%, respectively, which suggests that increases in pyrene content results in increases in the degree of sulfonation.

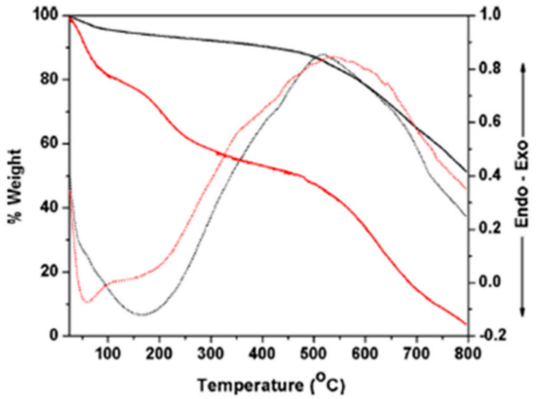


**Figure 7.** TGA and DTA traces of neat (black lines) and sulfonated POPs (red lines). Reproduced with permission from [61]. Copyright 2015, WILEY-VCH Verlag GmbH & Co.

The characterization techniques reviewed above facilitate the determination of nanoparticle dispersion and size, surface morphology and area, porosity, the adsorption bands of the functional groups present, phase composition, thermal stability, elemental composition, and the structures of the nuclei of the metal-encapsulated and functionalized POPs. For accurate characterization of POP-based materials, the techniques described above should not be used separately but preferably in complementary ways.

## 5. Catalytic Applications of Metal-encapsulated Porous Organic-Polymer Nanocatalysts

In this section, we review the catalytic activities of various metal-encapsulated and functionalized POPs. The recent literature reveals that heterogeneous catalysts can be synthesized through the immobilization and fabrication of nanoparticles within the nanoporous network of the porous organic polymer, and then used for aerobic oxidation, hydrogenation, coupling, and acid-catalyzed reactions, among other applications and the summary of results are shown in Table 4.

**Table 4.** Catalytic activity of supported metal nanoparticles and functionalized porous organic polymers.

| Material | Substrate | Catalyzed Reactions | Ref. |
|---|---|---|---|
| Pd@CPPF1 and Pd@CPPF2 | Olefins | Hydrogenation | [59] |
| Pd@CPPC and Pd@CPPY | Olefins | Hydrogenation | [57] |
| Pd@CPP1 and Pd@CPP2 | Nitroarene | Hydrogenation | [58] |
| Pd@OIP1 and Pd@OIP2 | Nitroarene | Hydrogenation | [56] |
| Ru-A, Ru-B, Ru-C | Nitroarene | Catalytic transfer hydrogenation | [51] |
| Cu-B | Aryl halides | Ullmann coupling | [52] |
| Pd-MPDVTA | Aryl halides | Heck cross coupling | [69] |
| Mn@DVTA1, Mn@DVTA2, Mn@DVTA1 | Aromatic hydrocarbons, alcohols | Aerobic C-H bond oxidation | [55] |
| $Mn_3O_4$@POP | Alkanols | Oxidation | [54] |
| SPPOP1, SPPOP2 and SPPOP3 | Fatty acids, esters, soybean and olive oils | Esterification and transesterification | [60] |
| SPPTPA | Carbohydrates | Dehydration | [61] |

### *5.1. Selective Hydrogenation Reactions*

#### 5.1.1. Hydrogenation Reactions

Hydrogenation is a chemical reaction in which the two hydrogen atoms of molecular hydrogen ($H_2$) react with another compound or element, and it usually takes place in the presence of a catalyst. It is normally used to reduce or saturate an organic compound. Non-catalytic hydrogenation is disadvantageous, as hydrogen is not reactive toward organic compounds unless high temperatures are used; therefore, these reactions normally require the use of a catalyst. The reduction of the double and triple bonds in hydrocarbons occurs at different temperatures and pressures, depending on the organic compound and the activity of the catalyst [70–72]. During hydrogenation, the unsaturated substrate is chemisorbed onto the catalyst, while hydrogen forms surface hydrides (M–H) with the catalyst that then transfers hydrogen to the chemisorbed substrate. Metals such as platinum, rhodium, palladium, and ruthenium have been reported to act as catalysts with excellent activity because they operate at lower temperatures and pressures. Non-precious nickel metal catalysts (e.g., Raney and Urishibara nickel) have emerged as economical alternatives, but the disadvantages of using higher temperatures with these catalysts makes the overall process more expensive [73,74].

Several palladium-incorporated POP catalysts have been used to hydrogenate olefins to their respective alkane products, as illustrated in Scheme 11 [57,59]. The catalytic activities of Pd@CPPF1

and Pd@CPPF2 were investigated through olefin hydrogenation at an olefin/Pd molar ratio of 1000 at 40 °C for 4 h under a pressure of 1.5 atm in the absence of a solvent. Olefins were completely converted into their respective products, confirming that the incorporation of Pd nanoparticles in the CPPF1 and CPPF2 POP supports enhance their catalytic activities toward olefins. Pd@CPPF1 and Pd@CPPF2 were further investigated for the hydrogenation of nitroarenes. When 0.1 mol% Pd@CPPF2 was used in the reaction, 15% conversion and 83% selectivity were obtained after 1 h. Increasing the reaction temperature from 25 to 40 °C resulted in increases in conversion and selectivity to 87% and 97%, respectively and increasing the palladium loading to 1 mol% resulted in the complete reduction of nitrobenzene, with aniline selectivity of 97% and 85% observed for the Pd@CPPF1 and Pd@CPPF2 catalysts, respectively. These results indicate that Pd@CPPF2 contains more active palladium species than Pd@CPPF1 as palladium nanoparticles with an average diameter of 6.7 nm were only monodispersed on the external surface of CPPF1, whereas small palladium nanoparticles with an average diameter of 3.4 nm were dispersed inside the pores of CPPF2. The hydrogenation of 1-hexene over the Pd@CPPC and Pd@CPPY catalysts under 1 atm of hydrogen at 25 °C was also investigated at an olefin/Pd molar ratio of 5000. The conversion of 1-hexene was 100% after 30 min, and 100% selectivity for n-hexane over both Pd@CPPC and Pd@CPPY was obtained after 90 and 60 min, respectively. A competition between the isomerization and hydrogenation of 1-hexene was observed, which hindered its simultaneous transformation into n-hexane over palladium nanoparticles, as the olefin-palladium intermediate can undergo either reductive elimination or $\beta$-H elimination to form hexene isomers. Pd@CPPY was shown to be more selective for hydrogenation than isomerization compared to other catalysts, suggesting that hydrogen diffusion into the palladium-particle clusters is facilitated by the use of ultrafine palladium nanoparticles. The catalytic activity of Pd@CPPY was further investigated with other olefins. 1-Octene was completely converted after 4 h; this conversion was significantly slower than that of hexane, indicating that alkene-chain length affects olefin reactivity. Reactivity was also affected by steric hindrance, as the hydrogenation of *trans*-2-octene was much slower than that of 1-octene. Styrene was fully hydrogenated in 30 min due to $\pi$–$\pi$ interactions between the styrene and aromatic structure of the porous polymer, as well as coordination of the styrene to the reachable surfaces of the ultrafine palladium nanoparticles. Pd@CPPY showed superior catalytic activity to Pd@CPPC due to its high surface area and large pore volume, which restricts nanoparticle aggregation. The above data demonstrate the applicability of flexible POPs as stable and tunable palladium-nanoparticle platforms in hydrogenation reactions with high conversion and selectivity.

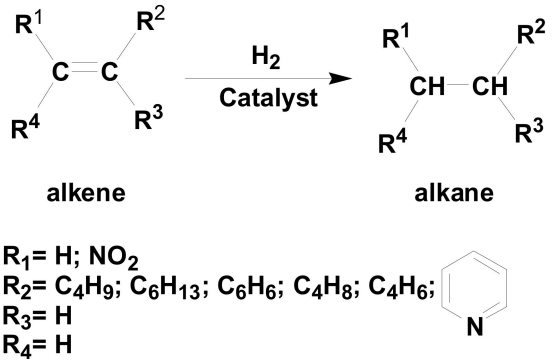


**Scheme 11.** Hydrogenation of olefins to alkanes.

### 5.1.2. Transfer Hydrogenation

Transfer hydrogenation involves the use of a hydrogen source other than gaseous hydrogen to add hydrogen to a molecule. Hydrogen sources such as organic molecules offer renewable substitutes for molecular hydrogen, which is flammable and stored at high pressures. These hydrogen donors reduce molecular chemical bonds with the aid of a catalyst through a process known as catalytic transfer hydrogenation (CTH) [75,76].

Mondal et al. [51] performed CTH on nitroarenes using POP-encapsulated Ru nanoparticles, as illustrated in Scheme 12. They found that stirring 0.05 mol of nitrobenzene with 5 mg of the Ru-A catalyst in EtOH for 12 h resulted in no conversion; however, the use of formic acid as a hydrogen donor in EtOH at 25 °C resulted in 52% conversion after 8 h. Increasing the reaction temperature to 80 °C led to 68% conversion after 6 h, while isopropyl alcohol as the hydrogen donor in DMF provided a 43% conversion after 6 h, and heating to 75 °C afforded a 70% conversion after 4 h. Glycerol in diglyme led to an 82% conversion at 125 °C after 4 h, and $H_2$ at room temperature and 1 bar of pressure resulted in an 85% conversion after 4 h. The CTH of nitrobenzene with $NaBH_4$ and the Ru-A catalyst in THF/$H_2O$ at room temperature resulted in a 92% conversion after 2.5 h. Increasing the amount of $NaBH_4$ to 1.5 and 2.5 mol led to conversions of 98% after 2 h and 0.5 h. The catalytic performance appeared to depend on the amount of catalyst, as conversions tended to increase with increasing amounts of catalyst; however, the product conversion was not substantial when a large amount of the catalyst was used. When Ru-BBA-1 was physically mixed, a lower catalytic activity (32%) was observed after 6 h compared to that obtained using the Ru-A catalyst under similar reaction conditions. Large crystalline particles of ruthenium incorporated on a porous organic-polymer support were more catalytically active compared to catalysts with smaller particles, indicating that large ruthenium nanoparticles interact well with the substrate through their larger numbers of exposed crystalline facets. These results reveal synergism between the highly cross-linked porous organic-polymer support and the ruthenium nanoparticles embedded inside and outside of the nanoporous network. High conversions were observed when $NaBH_4$ was used. $NaBH_4$ is a hazardous hydrogen donor; therefore, POP-based materials that use environmentally friendly hydrogen donors need to be developed.

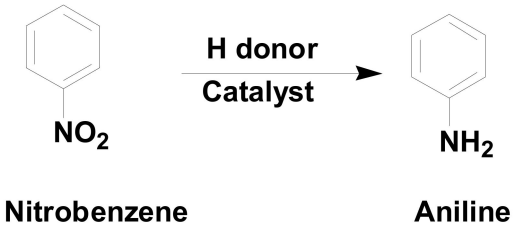


**Scheme 12.** Catalytic transfer hydrogenation of nitrobenzene to aniline.

5.1.3. Cross-Coupling Reactions

In organic chemistry, a coupling reaction involves the bonding of two molecular fragments aided by a metal catalyst. An organometallic compound RM, where R is an organic fragment and M is a main-group metal center, reacts with an organic halide (R'X) to form R-R', which contains a new carbon-carbon bond, as shown in Scheme 13 [77,78].


**Scheme 13.** Depicting a cross-coupling reaction.

5.1.4. C-N Bond-Forming Reactions

The Ullman coupling reaction of an aryl halide with an amine to form a C–N bond in the presence of a copper catalyst has received significant interest because the products formed can be used in pharmaceutical and other applications [79]. Under homogeneous conditions, these coupling reactions require expensive N- or P-ligands to sustain catalytic turnover. Consequently, heterogeneous catalysts are more promising for sustainable applications in which the catalyst is easily recovered and reused by simple filtration [80,81].

Mondal et al. [52] investigated the Ullman coupling reactions of aryl halides with amines, as shown in Scheme 14. The reaction of 4-iodoanisole with methylamine in the presence of $Cs_2CO_3$ and the Cu-A nanocatalyst at 110 °C resulted in a 64% catalytic conversion after 24 h, while the Cu-B catalyst, under the same reaction conditions, afforded an improved yield (76%) of *N*-methoxy-*N*-methylaniline

within 3 h. The reaction consistently provided yields of 80% on the large scale when the Cu-B catalyst was used, but the yield dropped to 53% when the base was changed to $K_2CO_3$, while no reaction was observed in the presence of $K_3PO_4$, $Et_3N$, or $Cs_2CO_3$. Bare $Cu^0$ nanoparticles resulted in a 50% conversion in 24 h, highlighting that the nanoporous polymer and the unique nanostructure of the Cu–B catalyst play vital roles that determine reaction efficiency. $Cu^0$ NPs loaded on carbon black exhibited a 50% yield after 24 h, while no product conversion was observed after 24 h when the nanoporous DVAC-1 polymer was used in the absence of Cu, suggesting that the copper nanoparticles are mainly responsible for the catalytic reaction. The Ullmann coupling of *meta*- and *ortho*-iodoanisoles gave 86% and 71% yields of the corresponding anilines, whereas 4-iodotoluene and 1-chloro-4-iodobenzene were converted in good yields into the corresponding anilines. The Cu-B catalyst displayed higher catalytic activity compared to other catalysts, which is ascribable to synergism between the high surface area and unique sea-urchin-like morphology that facilitates interactions between the active Cu sites and the substrate. These reactions take place at very high temperatures, which necessitates the preparation of POP-based catalysts that can perform at lower temperatures.

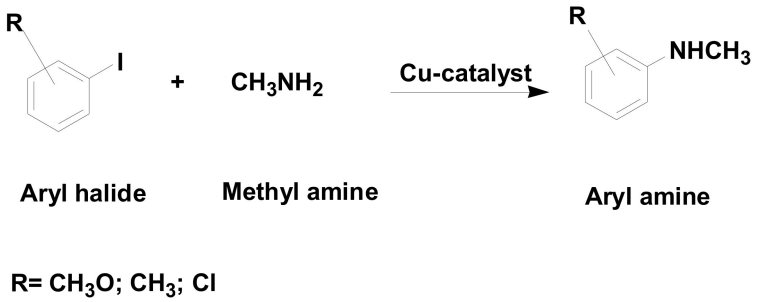


**Scheme 14.** Ullmann coupling reactions of aryl halides with amines.

#### 5.1.5. C–C Bond-Forming Reactions

Researchers are interested in C–C bond-forming reactions that can be used to prepare value-added organic target molecules [82]. The Heck reaction, which involves the reaction between an unsaturated halide and an alkene in the presence of a base and a palladium catalyst to form a substituted alkene, was the first example of a C–C bond-forming reaction. This reaction follows a Pd(0)/Pd(II) catalytic cycle, as is also seen in other Pd(0)-catalyzed cross-coupling reactions [83]. Gomes et al. [69] used a polymer-based palladium-grafted mesoporous catalyst (Pd-MPDVTA-1) to catalyze the Heck couplings of iodo, bromo, and chloroarenes in aqueous media, as illustrated in Scheme 15. The results revealed that Pd-MPDVTA is highly catalytically active, a consequence of the 5–10 nm palladium nanospheres uniformly embedded at the surface of the polymeric network. This chemical route required a high temperature (100 °C) to afford a high yield (86%).

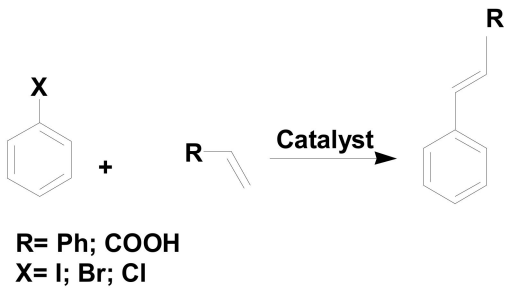


**Scheme 15.** Heck cross-coupling reactions of aryl halides and olefins.

### *5.2. Selective Oxidation Reactions*

Oxidation is an important industrial process technology that converts hydrocarbons into valuable oxygenated compounds. The reactivity and selectivity of an oxidant toward hydrocarbons in

autoxidation and metal-catalyzed oxidations have been studied extensively for gas- and liquid-phase oxidation reactions. According to the free-radical chain mechanism, oxidation proceeds via free-radical intermediates, and involves elementary steps that include chain initiation, chain propagation, and chain termination that characterize the overall process [84–86]. Mondal et al. [55] investigated the catalytic activities of morphologically different $Mn_3O_4$ samples incorporated in a DVTA nanoporous polymer as the catalysts for the aerobic oxidation of aromatic hydrocarbons, as illustrated in Scheme 16. Toluene was converted in 2% when the reaction was conducted using bare Mn NP-3 in the absence of the nanoporous polymer, which helped to determine the catalytically active sites, whereas the Mn@DVTA1, Mn@DVTA2, and Mn@DVTA3 nanocatalysts exhibited conversions of 2–32%. The Mn@DVTA1 nanocatalyst exhibited lower catalytic activity than bare Mn NP-3 due to its low surface area and poor crystallinity. Mn@DVTA2 and Mn@DVTA3 were oxidatively competitive; however, Mn@DVTA3 converted more toluene due to the incorporation of octahedral $MnO_3$ nanoparticles on the DVTA polymer. The higher catalytic activity observed for Mn@DVTA3 is due to its (101) crystallographic facets that are more exposed than the (100) facets that exist in low amounts and have low surface energies. The $Mn_3O_4$@$SiO_2$ and $Mn_3O_4$@C catalysts exhibited superior catalytic performance than bare $Mn_3O_4$ nanoparticles, but poorer than that of Mn@$DVTA_3$, which indicates that the polymer matrix plays a major role in these oxidation reactions, facilitating the easy diffusion of the organic substrate and its interactions with the catalytic $Mn_3O_4$ centers. The Mn@$DVTA_3$ nanocatalyst was explored for its ability to oxidize aromatic hydrocarbons in the absence of a solvent. Indane was oxidized into 1-indanole and 1-indanone in an overall conversion of 8% and with selectivity of 3% and 95%, respectively. The oxidations of ethylbenzene, diphenylmethane, and toluene proceeded in conversions of 12, 10, and 32%, respectively. Steric hindrance was observed to affect the rate of oxidation, as diphenylmethane reacted more slowly than ethylbenzene. These catalysts exhibited low substrate conversions and low product selectivity.

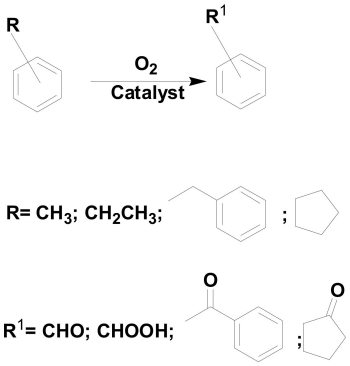


**Scheme 16.** Oxidations of aromatic hydrocarbons.

Dhanalaxmi et al. [54] also studied the catalytic activity of $Mn_3O_4$ NPs encapsulated in a triazine-based hybrid POP material for the aerobic oxidation of alcohols to carbonyl compounds at 80 °C [35], as shown in Scheme 17. Cyclohexylmethanol was transformed to the corresponding aldehyde in 97.9% conversion and with a TOF of 13.4 $h^{-1}$, while the oxidation of benzyl alcohol afforded benzaldehyde with a TOF of 4.6 $h^{-1}$. The oxidation of 9-fluorenemethanol proceeded in 76.2% conversion, while less-reactive cyclic alkanols were oxidized with high TOF values, irrespective of ring size. The cycloctanol with a larger ring was selectively oxidized to the corresponding ketone with a TOF of 8.6 $h^{-1}$. The $Mn_3O_4$@POP nanocatalyst was very active in large-scale oxidations and performed well during the oxidation of aliphatic; $\alpha$,$\beta$ unsaturated; substituted; and heterocyclic alcohols, which proceeded with high selectivity [54]. The nanocatalyst was very effective for the oxidation of cyclic alkanols to the corresponding ketones, and over-oxidized products were not observed. This impressive catalytic performance is attributable to the highly cross-linked organic rigid porous and well-defined 3D structure that facilitates the easy diffusion of the substrate to the more

exposed reactive sites in the cavities of the porous structure. Synergism between the C-N and Mn units of the catalyst resulted in increased interactions with alkanols and the activation of C-H, O-H, and O-O bonds.

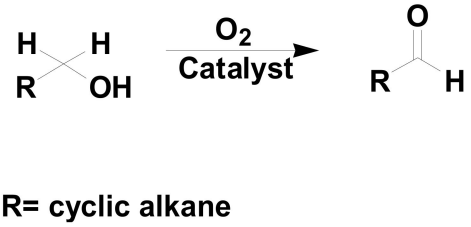


**Scheme 17.** Oxidations of cyclic alkanols to ketones.

### *5.3. Acid-Catalyzed Reactions*

#### 5.3.1. Esterification and Transesterification Reactions

Esterification and transesterification reactions are industrially important for the production of flavors, aromas, and biodiesel esters [87]. Kundu and Bhaumik [60] used SPPOP1, SPPOP2, and SPPOP3 as catalysts for the esterification and transesterification of fatty acids and esters, as illustrated in Scheme 18 for the preparation of long-chain mono- and dicarboxylic acids. The product yields increased in the order: SPPOP1 < SPPOP2 < SPPOP3, which reflects the order of catalyst acidity. The higher catalytic activity observed for SPPOP3 is due to the presence of more Brønsted-acid sites in the catalyst. The conversions of fatty acids into esters progressively increased with time, and reactions at higher temperatures required much less much time. The rate of the forward reaction was higher than that of the reverse reaction, and the yields of the corresponding methyl esters increased from 70 to 90% after 10 h, as the molar ratio of fatty acid to methanol was reduced from 1:5 to 1:50 [60].

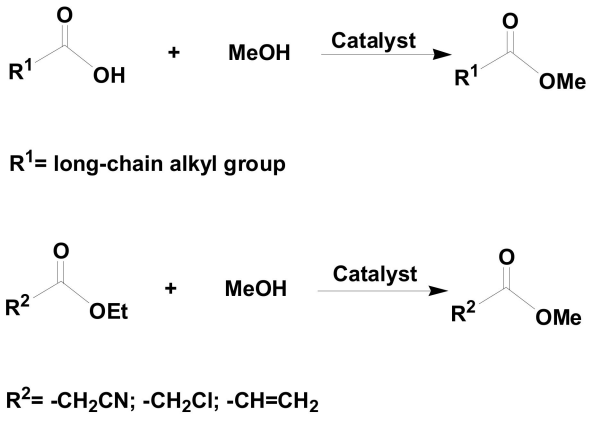


**Scheme 18.** Esterifications and transesterifications of fatty acids and esters.

Esterifications of free fatty acids usually require high temperatures and the presence of the homogeneous and hazardous $H_2SO_4$ catalyst [88], which is also difficult to separate from the reaction mixture [89]. Numerous porous solid acid catalysts have been reported for biofuel production; however, they all require high temperatures [90]. Porous sulfonated zinc and tin(IV) phosphonate materials were also reported for the room-temperature synthesis of biodiesel; this method was exceptional and green, but the synthesis of the catalysts was time consuming (2–3 d) [91,92].

#### 5.3.2. Dehydration Reactions

Dehydration is a chemical reaction that involves two compounds and produces water as one of the products. For example, when two monomers react, the proton from one monomer becomes attached to the hydroxyl group of the other monomer to form a dimeric product and a water molecule.

Brønsted-acid catalysts are used to protonate hydroxyl groups to form $–OH_2^+$, since the hydroxyl group itself is a poor leaving group [92]. Mondal et al. [61], used the SPPTPA-1 catalyst to form 5-(hydroxymethyl)furfural (HMF) by the dehydration of carbohydrates under microwave conditions, as shown in Scheme 19. The reaction was first performed at 120 °C to afford HMF in 90.3% yield after 20 min. Increasing the temperature from 120 °C to 130 °C, and then to 140 °C improved the HMF yield to 91.6% and 94.6%, respectively. Ionic liquids such as NMP and DMA-LiCl have been used as solvents instead of DMSO to give HMF in yields of 86.7% and 95.9%, respectively. The higher HMF yields obtained in NMP and DMSO are ascribable to their good microwave-absorbing abilities, and improved catalytic activities for the conversion of the glucopyranose into the fructofuranose at higher temperatures. The conversion of sucrose into HMF was also examined using the SPPTPA-1 catalyst, which afforded a 51.4% yield of HMF when treated at 140 °C in DMSO, while conversions of 49.5 and 31.4% were observed when treated for 10 and 20 min in DMA-Li as the solvent, respectively. HMF yields of 46.0 and 56.6% were obtained in 10 and 20 min, respectively, when NMP was used as the solvent for the conversion of sucrose. Sugarcane bagasse provided HMF in 18.8% yield in DMSO after 60 min under microwave irradiation, whereas a poor HMF yield of 4.5% was obtained in DMA-LiCl. The higher catalytic activity over shorter reaction times is due to the high surface area and large pore volume of the porous organic polymer that facilitate easy diffusion of the organic substrate into the pore channels. This diffusion helps the substrate to effectively interact with the active catalytic centers. These catalysts provided HMF in high yields over short times, but they required higher temperatures.

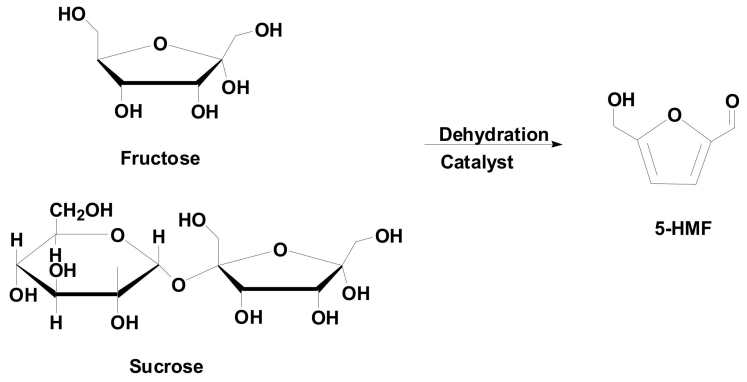


**Scheme 19.** Dehydration of carbohydrates to 5-(hydroxymethyl)furfural (HMF).

## 6. Comments on Catalyst Stability, Recyclability, and Deactivation

The recyclability and reusability of the functionalized and metal-encapsulated POPs were examined by separating the catalysts from the reaction mixtures by simple filtration following use. The collected catalysts were then washed with water/organic solvents and dried prior to re-use. The nanocatalysts were easily reactivated without the need for acid, base, or special treatment (i.e., calcination at higher temperature) [51–63]. The $Mn_3O_4$@POP nanocatalyst could be successfully recycled and reused for 3–15 consecutive cycles [54], which represents the highest catalyst recycling reported to date (Table 5). Hot filtration and leaching experiments revealed that these nanocatalysts are heterogeneous in nature, as the nanoparticle contents of the nanocatalysts after active catalytic cycling were found to be comparable to those of the fresh catalysts. This verifies that no nanoparticle leaching occurred during reaction and indicates that the nanoparticles are solidly entrapped inside the porous cavities of the polymeric frameworks [51–63]. Reused catalysts were also instrumentally characterized; EDX and elemental mapping revealed that a significant amount of ions had become adsorbed and trapped in the nanopores after active catalytic cycling, preventing the diffusion of organic substrates into the porous channels and, consequently, resulting in a decrease in catalytic activity. This was also verified by substantial decreases in BET surface areas and pore volumes, in which the clogged nanopores hindered the adsorption of nitrogen into the porous channels. XRD and XPS revealed that the phases and oxidation states of the nanoparticles on the various structures remained unchanged

following catalysis, while NMR spectroscopy was used to show that the organic functional groups in the nanoporous backbones remained structurally intact, and TEM showed no recognizable aggregation of nanoparticles, further verifying their high stabilities during catalysis [51–63]. The $NH_3$-TPD results for used sulfonated polymers suggest no changes in total acidity, confirming their stabilities and verifying that no leaching of the $–SO_3H$ groups occurred during the various reactions [61]. In contrast to previously reported catalysts, heterogeneous catalysts based on POPs exhibited remarkable catalytic performance, high chemical stability and reusability, with no sign of leaching, which is ascribable to the well-defined three dimensional highly cross-linked rigid porous organic structure that facilitates easy mass transfer and diffusion.

**Table 5.** Recyclability and reusability of metal encapsulated and functionalized POPs.

| Catalyst | No. of Catalytic Runs | Ref. |
|---|---|---|
| Ru-A | 10 | [51] |
| Cu-B | 5 | [52] |
| Mn@DVTA-3 | 5 | [53] |
| $Mn_3O_4$@POP | 15 | [54] |
| Pd@CPP-C | 4 | [57] |
| Pd@CPP-Y | 7 | [57] |
| Pd@CPP1 | 5 | [58] |
| Pd@CPP2 | 4 | [58] |
| Pd@CPP1-$NaBH_4$ | 3 | [58] |
| SPPTPA-1 | 4 | [61] |
| SPPOP-1 | 6 | [63] |

## 7. Conclusion and Future Outlook

Although POPs are chemically more stable than other framework materials, their amorphous nature and network-interpenetration tendencies contribute to their polydispersed pore distributions and surface areas that are not yet very high. The development of ordered POPs devoid of network interpenetration remains a major challenge that needs to be addressed. The use of rigid 3D building blocks is necessary in order to guarantee space-inefficient packing and porosity, which is also limited by the lack of structural diversity available through POP synthesis. Therefore, the choice of starting materials or procedures for the control of pore size and surface area during polymerization are problems that merit the attention of researchers interested in developing new POPs. The ability to produce size and shape selectivity at the molecular level by changing the steric environments of linkers is another challenge that requires attention. If the cross-linking reactions were reversible under the synthesis conditions, then bond-formation errors would be alleviated and POPs with uniform pores and thermodynamically stable structures could be obtained.

From the literature review, we conclude that interest in the development of POPs has increased due to the existence of effective platforms that incorporate active metal nanoparticles into their framework structures, which is ascribable to their chemical and thermal stabilities. Their binding abilities and versatile nature also make them attractive for application to heterogeneous catalysis that address challenges such as sustainability, cost, and ease of synthesis, especially for the large-scale synthesis of POPs for applications in numerous fields.

**Author Contributions:** W.S. wrote the first draft of manuscript and S.S.R. critically reviewed and corrected the manuscript.

**Funding:** The authors are grateful to the Department of Science and Technology (DST, project no. HGERA8X) and the Council for Scientific and Industrial Research (CSIR, project no. HGER74p) of South Africa for financial support.

**Acknowledgments:** The authors would like to thank the Department of Science and Technology (HGERA8X) and the Council for Scientific and Industrial Research (HGER74P), South Africa for financial support.

**Conflicts of Interest:** The authors declare no conflict of interest.

## References


1. Perego, C.; Millini, R. Porous materials in catalysis: Challenges for mesoporous materials. *Chem. Soc. Rev.* **2013**, *42*, 3956–3976. [CrossRef] [PubMed]
2. Sun, Q.; Dai, Z.; Meng, X.; Wang, L.; Xiao, F.S. Task specific design of porous polymer heterogeneous catalysts beyond homogeneous counterparts. *ACS. Catal.* **2015**, *5*, 4556–4567. [CrossRef]
3. Ding, S.Y.; Gao, J.; Wang, Q.; Zhang, Y.; Song, W.G.; Su, C.Y.; Wang, W. Construction of covalent organic framework for catalysis: Pd/COF-LZU1 in Suzuki-Miyaura coupling reaction. *J. Am. Chem. Soc.* **2011**, *133*, 19816–19822. [CrossRef] [PubMed]
4. Li, L.; Chen, Z.; Zhong, H.; Wang, R. Urea-based porous organic frameworks: Effective supports for catalysis in neat water. *Chem. Eur. J.* **2014**, *20*, 3050–3060. [CrossRef] [PubMed]
5. Burda, C.; Chen, X.; Narayanan, R.; El-Sayed, M.A. Chemistry and properties of nanocrystals of Different shapes. *Chem. Rev.* **2005**, *105*, 1025–1102. [CrossRef] [PubMed]
6. Vajda, S.; Pellin, M.J.; Greeley, J.P.; Marshall, C.L.; Curtiss, L.A.; Ballentine, G.A.; Elam, J.W.; Catillon-Mucherie, S.; Redfern, P.C.; Mehmood, F. Subnanometre platinum clusters as highly active and selective catalysts for the oxidative dehydrogenation of propane. *Nat. Mater.* **2009**, *8*, 213–216. [CrossRef] [PubMed]
7. Qiao, B.; Wang, A.; Yang, X.; Allard, L.F.; Jiang, Z.; Cui, Y.; Liu, J.; Li, J.; Zhang, T. Single-atom catalysis of CO oxidation using Pt1/FeOx. *Nat. Chem.* **2011**, *3*, 634–641. [CrossRef] [PubMed]
8. Li, Z.; Liu, J.; Xia, C.; Li, F. Nitrogen-functionalized ordered mesoporous carbons as multifunctional supports of ultrasmall Pd nanoparticles for hydrogenation of phenol. *ACS Catal.* **2013**, *3*, 2440–2448. [CrossRef]
9. Kibata, T.; Mitsudome, T.; Mizugaki, T.; Jitsukawa, K.; Kaneda, K. Investigation of size-dependent properties of sub-nanometer palladium clusters encapsulated within a polyamine dendrimer. *Chem. Commun.* **2013**, *49*, 167–169. [CrossRef] [PubMed]
10. White, R.J.; Luque, R.; Budarin, V.L.; Clark, J.H.; Macquarrie, D.J. Supporetd metal nanoparticles on porous materials: Methods and applications. *Chem. Soc. Rev.* **2009**, *38*, 481–494. [CrossRef] [PubMed]
11. Kaur, P.; Hupp, J.T.; Nguyen, S.T. Porous organic polymers in catalysis: Opportunities and challenges. *ACS Catal.* **2011**, *1*, 819–835. [CrossRef]
12. Mckeown, N.B.; Budd, P.M. Polymers of intrinsic microporosity (PIMs): Organic materials for membrane separations, heterogeneous catalysis and hydrogen storage. *Chem. Soc. Rev.* **2006**, *35*, 675–683. [CrossRef] [PubMed]
13. Cooper, A.I. Conjugated microporous polymers. *Adv. Mater.* **2009**, *21*, 1291–1295. [CrossRef]
14. Wang, Z.; Chem, G.; Ding, K.L. Self-supported catalysts. *Chem. Rev.* **2009**, *109*, 322–359. [CrossRef] [PubMed]
15. Trewin, A.; Cooper, A.I. Porous organic polymers: Distinction from disorder? *Angew. Chem. Int. Ed.* **2010**, *49*, 1533–1535. [CrossRef] [PubMed]
16. Jiang, J.X.; Su, F.B.; Trewin, A.; Wood, C.D.; Campbell, N.L.; Niu, H.J.; Dickson, C.; Ganin, A.Y.; Rosseinsky, M.J.; Khimyak, Y.Z.; et al. Conjugated microporous poly (aryleneethynylene) networks. *Angew. Chem. Int. Ed.* **2007**, *46*, 8574–8578. [CrossRef] [PubMed]
17. Schmidt, J.; Weber, J.; Epping, J.D.; Antonietti, M.; Thomas, A. Microporous conjugated poly(thienylene arylene) networks. *Adv. Mater.* **2009**, *21*, 702–705. [CrossRef]
18. Ben, T.; Ren, H.; Ma, S.Q.; Cao, D.; Lan, J.H.; Jing, X.F.; Wang, W.C.; Xu, J.; Deng, F.; Simmons, J.M.; et al. Targeted synthesis of a porous aromatic framework with high stability and exceptionally high surface area. *Angew. Chem. Int. Ed.* **2009**, *48*, 9457–9460. [CrossRef] [PubMed]
19. Chen, L.; Honsho, Y.; Seki, S.; Jiang, D.L. Light-harvesting conjugated microporous polymers: Rapid and high efficient flow of light energy with aporous polyphenylene framework as antenna. *J. Am. Chem. Soc.* **2010**, *132*, 6742–6748. [CrossRef] [PubMed]
20. Wu, C.D.; Hu, A.; Zhang, L.; Lin, W.B. Homochiral porous metal organic framework for highly enantioselective heterogeneous asymmetric catalysis. *J. Am. Chem. Soc.* **2005**, *127*, 8940–8941. [CrossRef] [PubMed]
21. Song, F.J.; Wang, C.; Falkowski, J.M.; Ma, L.Q.; Lin, W.B. Isoreticular chiral metal-organic frameworks for asymmetric alkene epoxidation: Tuning catalytic activity by controlling framework catenation and varying open channel sizes. *J. Am. Chem. Soc.* **2010**, *132*, 15390–15398. [CrossRef] [PubMed]

22. Ding, S.Y.; Wang, W. Covalent organic frameworks (COFs): From design to applications. *Chem. Soc. Rev.* **2013**, *42*, 548–568. [CrossRef] [PubMed]
23. Feng, X.; Ding, X.S.; Jiang, D.L. Covalent organic frameworks. *Chem. Soc. Rev.* **2012**, *41*, 6010–6022. [CrossRef] [PubMed]
24. Wang, T.; Lyu, Y.; Xiong, K.; Wang, W.; Zhang, H.; Zhan, Z.; Jiang, Z.; Ding, Y. Chiral BINAP-based hierarchical porous polymers as platforms for efficient heterogeneous asymmetric catalysis. *Chin. J. Catal.* **2017**, *38*, 890–898. [CrossRef]
25. Wang, W.; Zheng, A.; Zhao, P.; Xia, C.; Li, F. Au-NHC@Porous organic polymers: Synthetic control and its catalytic application in alkyne hydration reactions. *ACS. Catal.* **2014**, *4*, 321–327. [CrossRef]
26. Dawson, R.; Cooper, A.I.; Adams, D.J. Nanoporous organic polymer networks. *Prog. Polym. Sci.* **2012**, *37*, 530–563. [CrossRef]
27. Zou, X.; Rena, H.; Zhu, G. Topology directed design of porous organic frameworks and their advanced applications. *Chem. Commun.* **2013**, *49*, 3925–3936. [CrossRef] [PubMed]
28. Suresh, V.M.; Bonakala, S.; Atreya, H.S.; Balasubramanian, S.; Maji, T.K. Amide functionalized microporous organic polymer for selective CO2 sorption and catalysis. *ACS. Appl. Mater. Interfaces* **2014**, *6*, 4630–4637. [CrossRef] [PubMed]
29. Fang, Q.; Gu, S.; Zheng, J.; Zhuang, Z.; Qui, S.; Yan, Y. 3D Microporous base functionalized covalent organic frameworks for size selective catalysis. *Angew. Chem. Int. Ed.* **2014**, *52*, 2878–2882. [CrossRef] [PubMed]
30. Zhang, Y.G.; Riduan, S.N. Functional porous organic polymers for heterogeneous catalysis. *Chem. Soc. Rev.* **2012**, *41*, 2083–2094. [CrossRef] [PubMed]
31. Zahmakirana, M.; Ozkar, S. Metal nanoparticles in liquid phase catalysis: From recent advances to future goals. *Nanoscale* **2011**, *3*, 3462–3481. [CrossRef] [PubMed]
32. Islam, N.; Miyazaki, K. Nanotechnology systems of innovation: Investigations of scientific disciplines fusion trend into nanotech. *PICMET* **2007**, *1*, 2922–2931.
33. Cooper, A.I.; De Simone, J.M. Polymer synthesis and characterization in liquid/supercritical carbon dioxide. *Curr. Opin. Solid State Mater. Sci.* **1996**, *1*, 761–768. [CrossRef]
34. Budd, P.M.; Ghanem, B.S.; Makhseed, S.; McKeown, N.B.; Msayib, K.J.; Tattershall, C.C. Polymer of intrinsic microporosity (PIMS): Robust, solution-processable, organic nanoporous materials. *Chem. Commun.* **2004**, 230–231. [CrossRef] [PubMed]
35. Vlakh, E.G.; Maksimova, E.F.; Krasikov, V.D.; Tennikova, T.B. Macroporous polymer materials: Synthesis of a new functional copolymer and its use for biological macroanalysis. *Polym. Sci.* **2009**, *51*, 1677–1685. [CrossRef]
36. Jiang, J.X.; Cooper, A.I. Microporous organic polymers: Design, synthesis and function. *Top. Curr. Chem.* **2010**, *293*, 1–33. [PubMed]
37. Ben, T.; Pei, C.; Zhang, D.; Xu, J.; Deng, F.; Jing, X.; Qui, S. Gas storage in porous aromatic frameworks (PAFs). *Energy Environ. Sci.* **2011**, *4*, 3991–3999. [CrossRef]
38. Hauser, B.G.; Farha, O.K.; Exley, J.; Hupp, J.T. Thermally enhancing the surface areas of Yamamoto-derived porous organic polymers. *Chem. Mater.* **2013**, *25*, 12–16. [CrossRef]
39. Li, B.; Zhang, Y.; Ma, D.; Shi, Z.; Ma, S. Mercury nano-trap for effective and efficient removal of mercury(II) from aqueous solution. *Nat. Commun.* **2014**, *5*, 5537. [CrossRef] [PubMed]
40. Long, P.; Qi, C.; Jian-Hua, Z.; Jian-Guo, Y.; Yu-Jian, H.; Bao-Hang, H. Hypercrosslinked porous polycarbazoles via one-step oxidative coupling reaction and Friedel-Crafts alkylation. *Polym. Chem.* **2015**, *6*, 2478–2487.
41. Zhang, P.; Weng, Z.; Guo, J.; Wang, C. Solution-dispersible, colloidal, conjugated porous polymer networks with entrapped palladium nanocrystals for heterogeneous catalysis of the Suzuki-Miyaura coupling reaction. *Chem. Mater.* **2011**, *2*, 5243–5249. [CrossRef]
42. Chen, L.; Yang, Y.; Jiang, D. CMPs as scaffolds for constructing porous catalytic frameworks: A built-in heterogeneous catalyst with high activity and selectivity based on nanoporous metalloporphyrin polymers. *J. Am. Chem. Soc.* **2010**, *132*, 9138–9143. [CrossRef] [PubMed]
43. Germain, J.; Hradil, J.; Frechet, J.M.J.; Svec, F. High surface area nanoporous polymers for reversible hydrogen storage. *Chem. Mater.* **2006**, *18*, 4430–4435. [CrossRef]
44. Qiao, Z.A.; Chai, S.H.; Nelson, K.; Bi, Z.; Chen, J.; Mahurin, S.M.; Zhu, X.; Dai, S. Polymeric molecular sieve membranes via in situ cross-linking of non-porous polymer membrane templates. *Nat. Commun.* **2014**, *5*, 3705. [CrossRef] [PubMed]

45. Li, B.; Guan, Z.; Wang, W.; Yang, X.; Hu, J.; Tan, B.; Li, T. Multifunctional microporous organic polymers. *Adv. Mater.* **2012**, *24*, 3390–3395. [CrossRef] [PubMed]
46. Kuhn, P.; Antonietti, M.; Thomas, A. Porous, covalent triazine-based frameworks prepared by ionothermal synthesis. *Angew. Chem. Int. Ed.* **2008**, *47*, 3450–3453. [CrossRef] [PubMed]
47. Chan-Thaw, C.E.; Villa, A.; Katekomol, P.; Su, D.; Thomas, A.; Prati, L. Covalent triazine framework as catalytic support for liquid phase reaction. *Nano Lett.* **2010**, *10*, 537–541. [CrossRef] [PubMed]
48. Xie, Z.; Wang, C.; deKrafft, K.E.; Lin, W. High stable and porous cross-linked polymers for efficient photocatalysis. *J. Amer. Chem. Soc.* **2011**, *133*, 2056–2059. [CrossRef] [PubMed]
49. Totten, R.K.; Weston, M.H.; Park, J.K.; Farha, O.K.; Hupp, J.T.; Nguyen, S.T. Catalytic solvolytic and hydrolytic degradation of toxic methyl paraoxon with La(catecholate)-functionalized porous organic polymers. *ACS Catal.* **2013**, *3*, 1454–1459. [CrossRef]
50. Gopalakrishnan, D.; Dichtel, W.R. Direct detection of RDX vapor using a conjugated polymer network. *J. Am. Chem. Soc.* **2013**, *135*, 8357–8362. [CrossRef] [PubMed]
51. Mondal, J.; Kundu, S.K.; Ng, W.K.N.; Singuru, R.; Borah, P.; Hirao, H. Fabrication of ruthenium nanoparticles in porous organic polymers: Towards advanced heterogeneous catalytic nanoreactors. *Chem. Eur. J.* **2015**, *21*, 19016–19027. [CrossRef] [PubMed]
52. Mondal, J.; Biswas, A.; Chiba, S.; Zhao, Y. Cu0 nanoparticles deposited on nanoporous polymers: A recyclable heterogeneous nanocatalysts for Ullmann coupling of aryl halides with amines in water. *Sci. Rep.* **2015**, *5*, 8294. [CrossRef] [PubMed]
53. Mondal, J.; Trinh, Q.T.; Jana, A.; Ng, W.K.H.; Borah, P.; Hirao, H.; Zhao, Y. Size-dependent catalytic activity of palladium nanoparticles fabricated in porous organic polymers for alkene hydrogenation at room temperature. *ACS App. Mater. Interfaces* **2016**, *8*, 15307–15319. [CrossRef] [PubMed]
54. Dhanalaxmi, K.; Singuru, R.; Kundu, S.K.; Reddy, B.M.; Bhaumik, A.; Mondal, J. Strongly coupled $Mn_3O_4$-Porous organic polymer hybrid: A robust, durable and potential nanocatalysts for alcohol oxidation reactions. *RSC Adv.* **2016**, *6*, 36728–36735. [CrossRef]
55. Mondal, J.; Borah, P.; Sreejth, S.; Nguyen, K.T.; Han, X.; Ma, X.; Zhao, Y. Morphology-tuned exceptional catalytic activity of porous polymer supported Mn3O4 in aerobic sp3 C-H bond oxidation of aromatic hydrocarbons and alcohols. *ChemCatChem* **2014**, *6*, 3518–3529. [CrossRef]
56. Zhao, H.; Wang, Y.; Wang, R. In situ formation of well-dispersed palladium nanoparticles immobilized in imidazolium-based organic polymers. *Chem. Commun.* **2014**, *50*, 10871–10874. [CrossRef] [PubMed]
57. Li, L.; Zhao, H.; Wang, R. Tailored synthesis of porous organic polymers decorating ultrafine palladium nanoparticles for hydrogenation of olefins. *ACS Catal.* **2015**, *5*, 948–955. [CrossRef]
58. Li, L.; Zhao, H.; Wang, J.; Wang, R. Facile fabrication of ultrafine palladium nanoparticles with size and location control in Click-based porous organic polymers. *ACS Nano* **2014**, *8*, 5352–5364. [CrossRef] [PubMed]
59. Li, L.; Zhou, C.; Zhao, H.; Wang, R. Spatial control of palladium nanoparticles in flexible click-based porous organic polymers for hydrogenation of olefin and nitrobenzene. *Nano Res.* **2014**, *8*, 709–721. [CrossRef]
60. Kundu, S.K.; Bhaumik, A. Pyrene-based porous organic polymers as efficient catalytic support for the synthesis of biodiesel at room temperature. *ACS Sustain. Chem. Eng.* **2015**, *3*, 1715–1723. [CrossRef]
61. Mondal, S.; Mondal, J.; Bhaumik, A. Sulfonated porous organic polymeric nanofibers as an efficient solid acid catalyst for the production of 5-Hydroxymethyl furfural from biomass. *ChemCatChem* **2015**, *7*, 3570–3578. [CrossRef]
62. Dhanalaxmi, K.; Singuru, R.; Modal, S.; Bai, L.; Reddy, B.M.; Bhaumik, A.; Mondal, J. Magnetic nanohybrid decorated porous organic polymer: Synergistic catalyst for high performance levulinic acid hydrogenation. *ACS Sustain. Chem. Eng.* **2017**, *5*, 8061–8069. [CrossRef]
63. Zhong, H.; Liu, C.; Zhou, H.; Wang, Y.; Wang, R. Prefunctionalized porous organic polymers: Effective supports of surface palladium nanoparticles for the enhancement of catalytic performances in dehalogenation. *Chem. Eur. J.* **2016**, *22*, 12533–12541. [CrossRef] [PubMed]
64. Luykx, D.M.A.M.; Peters, R.J.B.; Van Ruth, S.M.; Bouwmeester, H. A review of analytical methods for the identification and characterization of nano delivery systems in food. *J. Agric. Food Chem.* **2008**, *56*, 8231–8247. [CrossRef] [PubMed]
65. Goldstein, J.; Newbury, D.; Joy, D.; Lyman, C.; Echlin, P.; Lifshin, E.; Sawyer, L.; Michael, J. *Scanning Electron Microscope and X-ray Microanalysis*; Kluwer Academic/Plenum Publishers: New York, NY, USA, 2003.

66. Reimer, L. Scanning Electron Microscopy, Physics of Image Formation and Microanalysis. Hawkes, P.W., Ed.; Springer: Berlin, Germany, 1998.
67. Wang, Z.L. Transmission electron microscopy of shape controlled nanocrystals and their assemblies. *J. Phys. Chem.* **2000**, *104*, 1153–1175. [CrossRef]
68. Williams, D.B.; Carter, C.B. *Transmission Electron Microscopy, a Textbook for Materials Science*; Plenum Press: New York, NY, USA, 1996.
69. Mondal, J.; Gomes, R.; Modak, A.; Bhaumik, A. Pd-anchored functionalized mesoporous materials as robust and recyclable heterogeneous catalysts for a series of C–C bond forming reactions. *Recycl. Catal.* **2013**, 10–33. [CrossRef]
70. Hudlicky, M. *Reductions in Organic Chemistry*, 2nd ed.; ACS: Washington, DC, USA, 1996; 429p.
71. Rylander, P.N. *Hydrogenation and Dehydrogenation in Ullmann's Encyclopedia of Industrial Chemistry*; Wiley-VCH: Weinheim, Germany, 2005.
72. Patel, D.R.; Ram, R.N. Hydrogenation of nitrobenzene using polymer bound Ru(III) complexes as catalyst. *Indian J. Chem. Technol.* **2000**, *7*, 280–285.
73. Allen, C.F.H.; Van Allan, J. M-toylybenzylamine. *Org. Synth.* **1995**, *3*, 827.
74. Mekler, A.B.; Ramachandran, S.; Swaminathan, S.; Newman, M.S. 2-Methyl-1–3-cyclohexanedione. *Org. Synth.* **1973**, *5*, 743.
75. Gilkey, M.J.; Xu, B. Heterogeneous catalytic transfer hydrogenation as an effective pathway in biomass upgrading. *ACS Catal.* **2016**, *6*, 1420–1436. [CrossRef]
76. Kilian, M. Bifunctional metal-ligand catalysis: Hydrogenation and new reactions within the metal-(Di)amine scaffold13. *Angew. Chem. Int. Ed.* **2005**, *44*, 6622–6627.
77. Dong, Z.; Ye, Z. Reusable, highly active heterogeneous palladium catalyst by convenient self-encapsulation cross-linking polymerisation for multiple carbon cross-coupling reactions at ppm to ppb palladium loadings. *Adv. Synth. Catal.* **2014**, *356*, 3401–3414. [CrossRef]
78. Brown, J.M. New trends in cross-coupling: Theory and applications. *Angew. Chem. Int. Ed.* **2015**, *54*, 5003. [CrossRef]
79. Senra, J.D.; Aguiar, L.C.S.; Simas, A.B.C. Recent progress in transition-metal catalyzed C-N cross-couplings: Emerging approaches towards sustainability. *Curr. Org. Synth.* **2011**, *8*, 53–78. [CrossRef]
80. Baqi, Y.; Mueller, C.E. Synthesis of alkyl- and aryl-amino-substituted anthraquinone derivatives by microwave-assisted copper(0)-catalyzed Ullmann coupling reactions. *Nat. Protoc.* **2010**, *5*, 945–953. [CrossRef] [PubMed]
81. Fanta, P.E. The Ullmann synthesis of biaryls. *Synthesis* **1974**, *38*, 139–196. [CrossRef]
82. Carme, D. In names, history and legacy. *Chem. Eng. News* **2010**, *88*, 31.
83. Sheldon, R.A. *Metal-Catalyzed Oxidation of Organic Compounds*; Sheldon, R.A., Kochi, J.K., Eds.; Academic Press: New York, NY, USA, 1981.
84. Suresh, A.K.; Sharm, M.M.; Sridhar, T. Engineering aspects of industrial liquid phase air oxidation of hydrocarbons. *Ind. Chem. Eng. Res.* **2000**, *29*, 3958–3997. [CrossRef]
85. Franz, G.; Sheldon, R.A. Oxidation in Ullmans encyclopedia of industrial chemistry. *VCH Verlagsgesellschaft* **1991**, *18*, 277–280.
86. Villeneuve, P.; Muderhwa, J.M.; Graille, J.; Haas, M.J. Customizing lipases for biocatalysis: A survey of chemical, physical and molecular biological approaches. *J. Mol. Catal. B Enzym.* **2000**, *9*, 113–148. [CrossRef]
87. Bojan, S.B.; Durairaj, S.K. Producing biodiesel from high free fatty acid jatropha curcas oil by a two step method-an Indian case study. *J. Sustain. Energy Environ.* **2012**, *3*, 63–66.
88. Tariq, M.; Ali, S.; Khalid, N. Activity of homogeneous and heterogeneous catalysts, spectroscopic and chromatographic characterization of biodiesel: A review. *Renew. Sustain. Energy Rev.* **2012**, *16*, 6303–6316. [CrossRef]
89. Zabeti, M.Z.; Wan Daud, W.M.A.; Aroua, M.K. Activity of solid catalysts for biodiesel production: A review. *Fuel Process. Technol.* **2009**, *90*, 770–777. [CrossRef]
90. Pramanik, M.; Nandi, M.; Uyama, H.; Bhaumik, A. Organic-inorganic hybrid porous sulfonated zinc phosphonate material: Efficient catalyst for biodiesel synthesis at room temperature. *Green Chem.* **2012**, *14*, 2273–2281. [CrossRef]

91. Dutta, A.; Patra, A.K.; Uyama, H.; Bhaumik, A. Template-free synthesis of a porous organic-inorganic hybrid Tin(IV) phosphonate and its high catalytic activity for esterification of free fatty acids. *ACS Appl. Mater. Interfaces* **2013**, *5*, 9913–9917. [CrossRef] [PubMed]
92. Friesen, J.B.; Schretzman, R. Dehydration of 2-methyl-1-cyclohexanol: New findings from a popular undergraduate laboratory experiment. *J. Chem. Educ.* **2011**, *88*, 1141–1147. [CrossRef]